FOI
SWEDISH DEFENCE
RESEARCH AGENCY

FOI-R--0281--SE
December 2001
ISSN 1650-1942
User report

Håkan Hansson, Peter Skoglund, Mattias Unosson

Structural protection for stationary/mobile tactical behaviour 2001

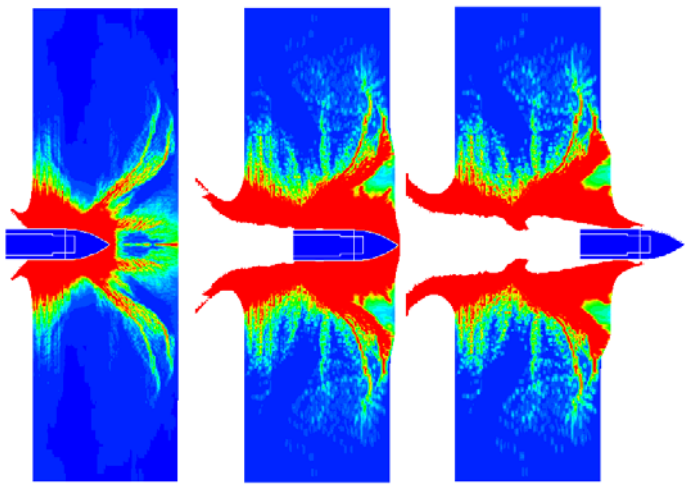

Weapons and Protection
SE-147 25 Tumba

SWEDISH DEFENCE RESEARCH AGENCY

Weapons and Protection
SE-147 25 Tumba

FOI-R--0281--SE

December 2001

ISSN 1650-1942

User report

Håkan Hansson, Peter Skoglund, Mattias Unosson

Structural protection for stationary/mobile tactical behaviour 2001

Issuing organization	Report number, ISRN	Report type
FOI – Swedish Defence Research Agency Weapons and Protection SE-147 25 Tumba	FOI-R--0281--SE	User report
	Research area code 5. Combat	
	Month year December 2001	**Project no.** E2011
	Customers code 5. Contracted Research	
	Sub area code 53 Protection and Fortification Techniques	

Author/s (editor/s)	Project manager
Håkan Hansson Peter Skoglund Mattias Unosson	Håkan Hansson
	Approved by
	Sponsoring agency Swedish defence HQ
	Scientifically and technically responsible

Report title

Structural protection for stationary/mobile tactical behaviour 2001

Abstract (not more than 200 words)

The activities for the project "Structural protection for stationary-mobile behaviour" during 2001 are reported here. The activities focus on the use of advanced material models and numerical simulations to describe structural behaviour during dynamic events, penetration in concrete and penetration of steel armour.

Numerical simulations of benchmark test with 152 mm projectiles were performed with the use of the RHT concrete model were performed. Comparisons are made between simulations performed with different element formulations (Lagrange, Euler and SPH), and the strengths as well as weaknesses of the formulations are discussed.

The concrete model developed by "Karagozian and Case" (K&C) was used for simulation of structural response, and the numerical results were compared with earlier test results from a series of impact loaded reinforced concrete beams.

Dynamic material testing to obtain the equation of state for high performance concrete (HPC) was conducted at EMI. The obtained material properties from the tests give an opportunity to perform more accurate simulations of concrete penetration in the future.

A study of the possibilities to determine penetration depths and ballistic limits for steel with the use of numerical models was conducted. The result from the simulation is in good agreement with the ballistic limit for the steel obtained by experiments.

Keywords

Numerical simulation, Euler, Lagrange, SPH, material behaviour, material properties, penetration, concrete, steel.

Further bibliographic information	Language English
ISSN 1650-1942	**Pages** 71 p.
	Price acc. to pricelist **Security classification**

Utgivare Totalförsvarets Forskningsinstitut - FOI Vapen och skydd 147 25 Tumba	**Rapportnummer, ISRN** FOI-R--0281--SE	**Klassificering** Användarrapport
	Forskningsområde 5. Bekämpning	
	Månad, år December 2001	**Projektnummer** E2011
	Verksamhetsgren 5. Uppdragsfinansierad verksamhet	
	Delområde 53 Skydd och anläggningsteknik	
Författare/redaktör Håkan Hansson Peter Skoglund Mattias Unosson	**Projektledare** Håkan Hansson	
	Godkänd av	
	Uppdragsgivare/kundbeteckning Försvarsmaktens högkvarter	
	Tekniskt och/eller vetenskapligt ansvarig	

Rapportens titel (i översättning)

Anläggningsskydd för fast-rörligt uppträdande 2001

Sammanfattning (högst 200 ord)

Denna rapport beskriver verksamheten inom projektet "Anläggningsskydd för fast-rörligt uppträdande" under 2001. Projektet har under detta år inriktats mot utvärdering av materialmodeller och numeriska verktyg för simulering av penetration i stål och betong, samt för strukturrespons hos betongkonstruktioner. Arbetet har även omfattat provning av material och beskrivning av materialens beteende.

Simuleringar av betongperforation baserade på tidigare genomförda ”benchmark”-försök med 152 mm projektiler har genomförts med en avancerad betongmodell utvecklad vid EMI. Vid dessa simuleringar har Lagrange-, Euler- och SPH-formulering använts och deras möjligheter, samt svagheter bedömts.

Betongmodellen utvecklad av "Karagozian and Case" (K&C) har använts för studie av stötbelastade strukturer. Simuleringar har jämförts med tidigare utförda stötbelastningar på armerade betongbalkar.

Materialprovning av högpresterande betong (HPC) har genomförts vid EMI för att bestämma dynamiska egenskaper vid höga tryck. Detta för att erhålla underlag till framtida numerisk simulering av penetration i betong.

En studie av möjligheterna att bedömma penetrationsdjup och ballistisk gränshastighet för stål med hjälp av numeriska modeller och framtagna materialdata har genomförts. Resultaten från simuleringarna stämmer bra överens med den experimentellt bestämda ballistiska gränshastigheten.

Nyckelord

Numerisk simulering, Euler, Lagrange, SPH, materialbeteende, materialegenskaper, penetration, betong, stål.

Övriga bibliografiska uppgifter	**Språk** Engelska
ISSN 1650-1942	**Antal sidor:** 71 s.
Distribution enligt missiv	**Pris: Enligt prislista** **Sekretess**

This page intentionally blank

CONTENTS

1. INTRODUCTION

The Swedish Armed Forces Headquarters finances the project “Structural protection for stationary and mobile tactical behaviour” at the Swedish Defence Research Agency (FOI). The overall goal for this project is to develop methods and techniques for modelling of weapons effects in order to provide a basis for the development of structural protection for stationary and mobile tactical behaviour.

The objectives for the project are to develop methodology and tools to predict and determine weapon effects on protective structures. Both experimental and theoretical research are used to develop and verify methods to optimise the protection levels of structures and other systems. The aim is to acquire knowledge that in the future can be used to design protective structures, and to develop new methods for protection. These future protective systems need to be adaptable for different environments, and different levels of the threats.

Modelling of materials subjected to weapons effects has been a major area of interest for a long time, and several material models to describe the material behaviour at high pressure and high strain rates are developed. However, it is not until recent years with the development of advanced material models that can be used together with the numerical formulations ALE, Euler or SPH formulations that it seems possible to model the behaviour of materials during penetration with an acceptable result.

This report focuses on the use of numerical models to describe structural behaviour during dynamic events, penetration in concrete and penetration in steel armour. The computer codes used for the simulations are LS-Dyna and Autodyn, with the structural response simulated with LS-Dyna and penetration simulations simulated with Autodyn. The concrete models developed by K&C (Karogozian and Case) and EMI (Ernst-Mach-Institut, Germany) were used to describe the material behaviour of concrete. The strength model developed by Johnson and Cook was used to describe the behaviour of steel during penetration. The material parameters have been determined for the used materials by mechanical testing for all cases, and the numerical results are compared with earlier obtained experimental data.

Some fundamental equations and definitions are compiled in the appendix to facilitate for the reader.

2. ACTIVITIES AND PUBLICATIONS DURING 2001

The activities during 2001 were focused on material behaviour and modelling of materials with application to structural response and penetration phenomena. A short description of the area of work is found below, and more information is given later in the report. For those further interested the recommendation is to study the other publications for the project, which are listed below.

Autodyn versions 4.1 and 4.2 were used together with the Johnson & Cook (J&C) material model to study the possibilities to model perforation of steel armour numerically. Strength parameters for the J&C model were determined from mechanical tests performed at FOI on high nitrogen alloyed steel (HNS) material and used for the simulations. Earlier performed ballistic tests with armour piercing small arms ammunition against HNS were used for comparison with the perforation simulations. It was shown that the ballistic limit of the HNS material was described by the model with an acceptable degree. However, the perforation models are very sensitive for the value of the used erosion strain in the material model for the Lagrange formulation. A numerical formulation with a fixed mesh or a mesh less formulation is necessary to avoid the problems caused by heavily distorted elements during penetration calculations. However, the meshless formulation SPH (Smooth Particle Hydrodynamics) was also used and this method was considered to be inadequate to describe the large tensile strains in the model during perforation. This resulted in a numerical failure without coupling to the physical material behaviour for the SPH models. Future studies of damage evolution and the use of fixed mesh formulations (Euler) are likely to enhance the accuracy of simulation of penetration in steels.

Perforation of concrete was studied with the use of Autodyn version 4.2 with the RHT model from EMI implemented. This material model shows promising behaviour for penetration/perforation simulations. However, the difficulties are to determine proper values for the material parameters to the model. This is discussed later in this report. Numerical simulations with Lagrange, Euler and SPH formulations were compared with earlier performed benchmark tests of projectile perforation of concrete.

Structural response was studied with the explicit FEM code LS-Dyna and the K&C (Karagozian and Case) material model. This model was earlier used to study air blast induced structural response at FOA, and the material model was further developed during the last year. Earlier performed drop weight tests on reinforced concrete beams were used for comparison with the numerical simulations. However, the model was not able to describe the local induced loading in the contact area of the concrete beam. The overall behaviour of the beam was on the other hand predicted with to acceptable degree.

At EMI a method to determine dynamic properties of mixtures is developed, and this method was used to determine properties of the high performance concrete (HPC) used by FOI. With this method it is possible to test the dynamic behaviour of the aggregate and the mortar for concrete, and thereafter calculate the behaviour of the mixed concrete. This simplifies the material testing of concrete at high pressures due to the possibility to use small test samples. To determine material properties of concrete it is otherwise necessary to use relatively large samples due the used aggregate size in the concrete. This results in both difficulties to obtain high loading pressures for static tests, and a wide scatter for the measured dynamic properties of the concrete. These material properties are necessary to obtain to be able to describe the behaviour of concrete for penetration simulations. The methodology to determine material properties of mixtures might also be useful to describe other types of material in the future.

Reports:

Hansson, H., Numerical simulation of concrete penetration with Euler and Lagrange formulations, FOI-R--0190--SE, Tumba, September 2001.

Hansson, H. and Skoglund, P., Modelling of steel behaviour with application to armour penetration, FOI-R--0201--SE, FOI, Tumba, December 2001.

Unosson, M., Modelling of concrete material behaviour with application to reinforced concrete beams subjected to impact, FOI-R--0167--SE, Tumba, October 2001.

Conference papers

Hansson, H., Numerical simulation of air blast, Proceedings of the 10th International symposium on interaction of the effects of munitions with structures, May 2001.

Magnusson, J. and Hallgren, M., High strength concrete beams subjected to shock waves from air blast - Experimental results, Proceedings of the 10th International symposium on interaction of the effects of munitions with structures, May 2001.

Unosson, M., Numerical simulation of the response of reinforced concrete beams subjected to heavy drop tests, 4th International Symposium on Impact Engineering, July 2001.

3. MODELLING OF STEEL BEHAVIOR WITH APPLICATION TO ARMOUR PENETRATION

A number of material models have been proposed to describe material behaviour with more or less complexity and physical background. In this study the Johnson and Cook (1983) strength model and Autodyn 2D were used to simulate material testing and perforation experiments. The implementations of the material models were verified by comparing the numerical solution of the flow stress for a simple steel cylinder subjected to different axial loads with the analytical solution given by the Johnson and Cook equation. It is found that the numerically calculated effect of strain rate on the flow stress deviates considerably from the analytical solution when the original implementation in Autodyn 2D version 4.1.13 is used. An improved implementation of the Johnson and Cook model developed by Westerling (2001) as a user routine was also compared with the analytical results. For this model there is an almost exact match between the numerical solution extracted from Autodyn and the analytical result. Further, both implementations were used for calculating the exit velocities for a tungsten carbide (WC) armour piercing 5.56 mm calibre projectile penetrating high nitrogen alloyed steel plates. Penetration phenomena involve very high and broad deformation rates. It is seen that the modified implementation of the Johnson and Cook equation gives a lower exit velocity and higher ballistic limit than the original implementation. The Autodyn 2D version 4.2.02 was released during this study, and this version includes a correction of the strain rate behaviour of the Johnson and Cook yield model. The calculated ballistic limit with the corrected version 4.2.02 of Autodyn is close to the one calculated with the user routine implemented at FOI and somewhat lower than the experimentally found limiting velocity.

3.1. The Johnson and Cook strength model

There are various models used to describe the strength of materials and one of the most frequently used equation for metals is the Johnson and Cook (1983) relation. This semi-empirical constitutive model was presented in 1983 and is used to describe the response of a number of metals. In equation 3.1 below the relation between flow stress σ (Pa), plastic strain ε, plastic strain rate $\dot{\varepsilon}$ (s^{-1}) and temperature T (K) suggested by Johnson and Cook (J&C) can be seen. The reference strain rate ($\dot{\varepsilon}_0$) is 1 s^{-1} and for strain rates below this value the strain rate enhancement are not used.

$$\sigma = \left(\sigma_0 + A\varepsilon^n\right)\left(1 + B\ln\frac{\dot{\varepsilon}}{\dot{\varepsilon}_0}\right)\left(1 - \left(\frac{T - T_r}{T_m - T_r}\right)^m\right) \qquad (3.1)$$

In this equation, T_r and $\dot{\varepsilon}_0$ is a reference temperature (usually room temperature) and reference strain rate (usually $1s^{-1}$) at which the material parameters σ_0 (Pa), A (Pa) and n are determined. The constant B in the second term takes the strain rate dependency into account. Finally, in the third term, T_m is the melting temperature and m is a parameter that includes the effect of temperature. It is noted that the influence of strain hardening (first term), strain rate (second term) and temperature (third term) are decoupled from each other. The equation above is for isothermal data, and for large strains and high strain rates the effect of adiabatic heating will complicate the evaluation of the material constants. Assuming that the deformation occurs isothermally, at the reference temperature, the third term in the equation equals 1. It is also noted that the contributions from strain rate and temperature are decoupled from each other, these effects are in reality more or less connected. Nevertheless, the model is generally accepted and is implemented in several finite element codes such as Autodyn.

3.2. Material properties for High Nitrogen alloyed Steel (HNS)

Nitrogen alloyed steels are interesting because they have a potential for high strength in connection with a high ductility. The high toughness is due to the austenitic, fcc, structure that these steels possess. Further, the nitrogen tends to stabilise the austenitic phase and thus increases the potential for improvement of strength by hardening without formation of martensite (Lach et al, 1997). Lach et. al (1997 and 1999) and Lichtenberg et. al (1997) have shown some very interesting results concerning the mechanical behaviour of such steels. Nitrogen alloyed steels have been known for some years but are still being developed and recent improvements in steel making technology has enabled the production of larger quantities. As a consequence the interest in nitrogen alloyed steels is increasing and a possible novel use for this type of material is for protective structures. The chemical composition of the material, kindly supplied by Columbus Steel, South Africa, can be seen in table 3.1.

Table 3.1. Chemical composition of the high nitrogen alloyed steel.

	C	Si	Mn	Cr	Ni	Mo	S	P	V	Ti	Cu	N
Suppliers data	0.08*	1.0*	9.50-11.0	18- 20	1.0*		0.015 *	0.045 *	-	-	-	0.4-0.6
Analysis	0.056	0.30	11.2	20.3	1.5	0.06	n/a	0.020	0.11	0.01	0.07	0.40

Note: * maximum

The mechanical characterisation of this steel was done at the FOI Research Centre at Grindsjön using samples with the geometry schematically shown in figure 2 below. A servo-hydraulic mechanical test frame was used for strain rates 10^{-3}, 10^{-2}, 1 and 10 s^{-1}. An instrumented pendulum impactor was used to measure the mechanical behaviour for the highest strain rates of 400 and 800 s^{-1}. This apparatus has been described in detail previously (Svensson, 1985). The stress-strain data collected at enhanced temperatures was taken using the servo-hydraulic testing device and an induction heater in connection with an IR-sensor and/or thermocouples to measure the temperature. Using this equipment, the mechanical properties of the HNS material at temperatures up to about 300 °C was measured.

A correction of the measured stress-strain data using a previously measured E-modulus of 196 GPa was done, see equation 3.2. Further, the plastic strain was defined to begin at a strain of 0.2% and the elastic part of the flow curve was subtracted according to relation 3.3.

$$e_{corr} = e_{tot} - S\left(\frac{1}{E_{app}} - \frac{1}{E_{true}}\right) \tag{3.2}$$

$$e_{pl} = e_{corr} - \left(\frac{S}{E_{true}} + 0.002\right) \tag{3.3}$$

In the equations above S and e_{tot} is the nominal stress and total nominal strain respectively. E_{app} is the apparent E-modulus (including machine stiffness etc.) while E_{true} is the separately determined true E-modulus. Finally the true flow stress curves were calculated for the uniform part of the deformation according to equations 3.4 and 3.5.

$$\varepsilon = \ln(1 + e_{pl}) \tag{3.4}$$

$$\sigma = S(e_{pl} + 1) \qquad (3.5)$$

In figures 3 and 4 below the extracted true plastic stress-strain curves is shown. In these figures the effect of increasing strain rate and temperature respectively on the flow stress is clear. Each curve shown in figure 3.1a are mean values of 2-4 experiments at room temperature, while the data at elevated temperatures in figure 3.1b are taken at constant strain rate (i.e. 1 s^{-1}) but different temperatures.

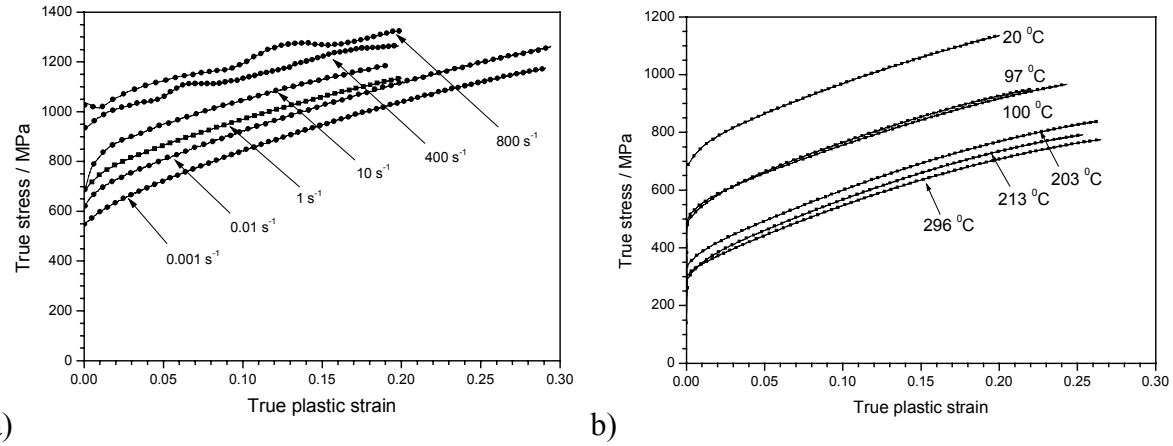

a) b)

Figure 3.1. Effect of strain rate at room temperature (a) and temperature at the strain rate 1 s^{-1} (b) on the flow stress for HNS.

From the data shown above parameters for the Johnson and Cook strength model can be extracted. A fit of the model to experimental results at the reference temperature and reference strain rate gives the yield stress (σ_0) and strain hardening constants A and n as seen in the first term of equation 3.1. The slope shown in figure 3.2a below corresponds to the strain rate parameter B in the model, while the temperature constant, m, in the third term is deduced from the line in figure 3.2b. It is assumed that the melting temperature equals 1793 K.

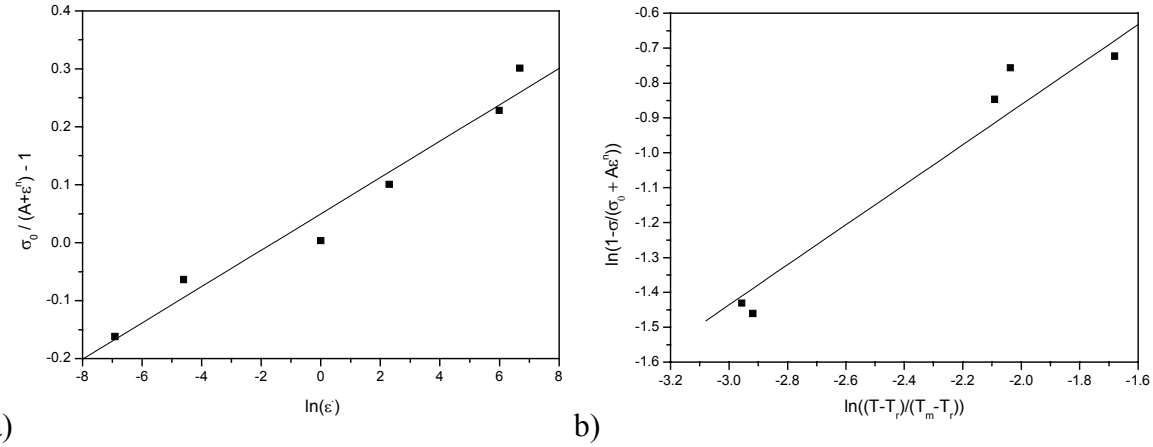

a) b)

Figure 3.2. The slopes correspond to the strain rate parameter B (a) and the temperature constant m (b) for the Johnson and Cook equation.

From the experiments the following Johnson and Cook strength model parameters are found. σ_0 = 682 MPa, A=1308 MPa, n= 0.657, strain rate enhancement B= 0.031 and temperature coefficient m=0.635. These figures differ slightly from the ones used for numerical calculations of the ballistic limit of 5.56 mm AP against an HNS plate (see table 3.2) and

previously published results (Skoglund and Savage, 2000). This deviation is due to the additional experimental work giving more data, which affects the averaging of the parameters. Using the two sets of parameters the calculated stress-strain curves gives a almost negligible difference. For example at a strain rate of 10^4 s^{-1}, a strain of 50% and a temperature of 200 °C the stress differs with about 3%, and thus is assumed to give a small effect on the overall penetration calculations.

The HNS material is very ductile and figure 3.3 show a representative geometry change before and after mechanical testing at room temperature. The diameter of the gauge part of the sample is 2 mm. The minimum diameter after fracture was measured, giving an average diameter close to 1.1 mm. As seen in the right diagram below the scatter is rather large and the standard deviation for the minimum fracture diameter is almost 0.2 mm. Samples fractured at nominal strain rates from 0.001 to 800 s^{-1} have been used for the calculations. No significant difference due to strain rate could be seen for this limited number of investigated samples.

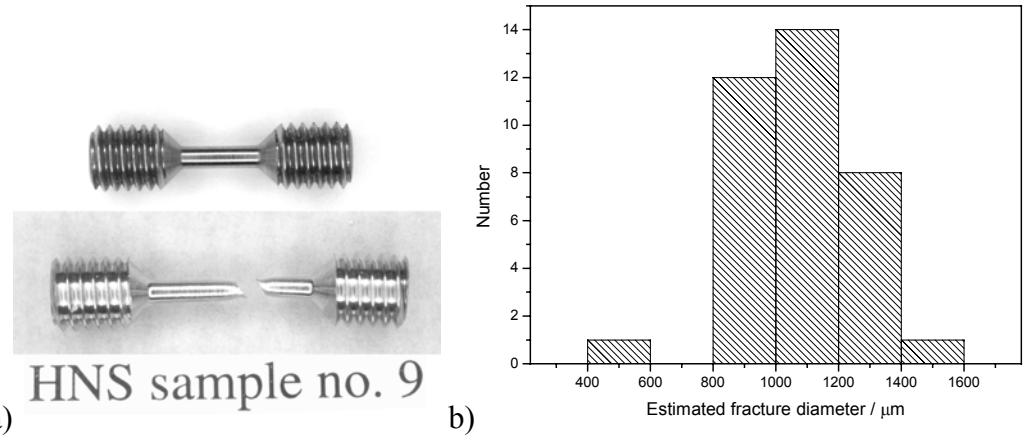

a) b)

Figure 3.3. Typical sample geometry before test and after fracture (a). The minimum diameter at fracture was measured giving an average value of 1.1 mm (b).

A maximum tensile fracture strain of 120% +- 40% is calculated with the use of the shown data in figure 3.3 and equation 3.6 (Dieter, 1988). This failure strain is later used as tensile fracture criteria for the numerical penetration calculation of a 5.56 mm AP against the HNS armour plate.

$$\varepsilon_{max} = \ln(A_0 / A_f) \qquad (3.6)$$

Where A_0 is the original area and A_f is the area after fracture.

3.3. Experimental results of penetration in HNS plates

Perforation tests on HNS plates were performed earlier at Åkers protection and FOI Research Centre Grindsjön. The results show that the HNS have the same level of protection as RHA steel, although the HNS material has lower yield strength. However, the HNS material also has a greater ductility (Savage et al, 1999). Only minor erosion is normally found for tungsten carbide cores after perforation of steel, and the plastic deformation of the projectile is normally negligible. Figure 3.4 show the experimental ballistic limit of the 5.56 mm AP against HNS and RHA steel plates, and the ballistic limit equals 762 m/s for 10.8 mm thick HNS plate. The experimental yield strength for the RHA was approximate 1200 MPa and for the HNS 650 MPa at a strain rate of 1 s^{-1}. The experimental procedure and ballistic results for the 5.56 mm AP and also 7.62 mm AP can be found in an earlier work (Savage et al, 1999).

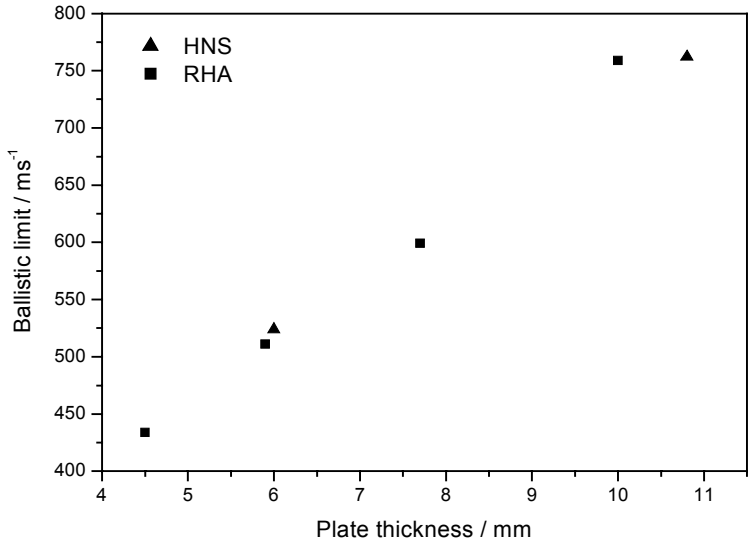

Figure 3.4. The ballistic limit against HNS (HB≈285) and RHA steel (HB≈300-320) plates of different thickness (Savage et al, 1999).

3.4. Numerical simulations

Two different types of numerical simulations were performed. First a simple axial tensile test of a steel cylinder, and then penetration of an armour piercing projectile in a steel plate. For these simulations both the 4340 and HNS steels were used. The simple tension test was performed to verify the implementations of the Johnson and Cook material strength model. The Autodyn 2D versions 4.1.13c and 4.2.02 were used for the numerical simulations. The material parameters used for 4340 and high nitrogen alloyed steel are shown in table 3.2. Other input data are a linear equation of state, principal tensile failure strain and erosion criteria for the Lagrange grid. A Lagrange mesh was used in most cases discussed and details concerning the different simulations can be seen below.

Table 3.2. Material data for HNS and 4340 steel used for simulation.

Input data for the steel materials		
Parameter	**HNS**	**4340**
Equation of state	Linear, with K=159 GPa	
Specific heat	477 J/kg K	
Density	7.83 g/cm^3	
Shear modulus	81.8 GPa	
Yield stress, σ_0	699 MPa	792 MPa
Strain hardening constant, A	1148 MPa	1148 MPa
Strain hardening exponent, n	0.595	0.26
Strain rate enhancement, B	0.030	0.014
Temperature exponent, m	0.65	1.03
Melting temperature, T_m	1793 K	

3.4.1. Simulation of tensile tests

A cylinder with length 4 mm and a radius of 1 mm with 0.2×0.2 mm element size was used for the tensile test simulations. 2D axial symmetry was used for the simulations, see figure 3.5. The left end of the cylinder was fixed, while the right end of the cylinder was subjected to different velocities giving nominal strain rates from 1 to 1000 s^{-1}. The shape of the loading pulse for the highest strain rate was slightly smoothened to avoid numerical effects of infinitely rise time of the loading pulse. This tensile test simulation was done in order to verify the implementation of the Johnson and Cook strength model.

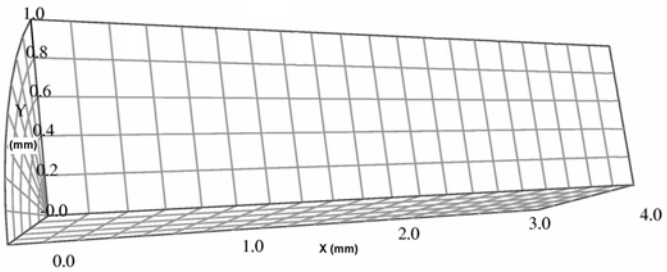

Figure 3.5. The cylindrical geometry used for the tensile test simulations. The rotational symmetry allows the use of a 2D model for the calculations.

An average stress for the mid cross section of the cylinder was determined for the different loading cases. Further, from the displacement of the right hand cylinder nodes a corresponding average axial strain for the cylinder can be calculated and in figure 3.6a the stress-strain relationship for the cylinder at different strain rates is shown. The resulting relationships are compared with the analytical solution of the Johnson and Cook flow stress using strains, strain rates and temperatures extracted from Autodyn, see figure 3.6b. As seen, the numerical solution differs greatly from the analytical solution at the higher strain rates. For this implementation of the Johnson and Cook model in Autodyn 2D version 4.1.13c the flow stress is almost unaffected of strain rate and remains at values close to the reference strain rate, i.e. 1 s^{-1}.

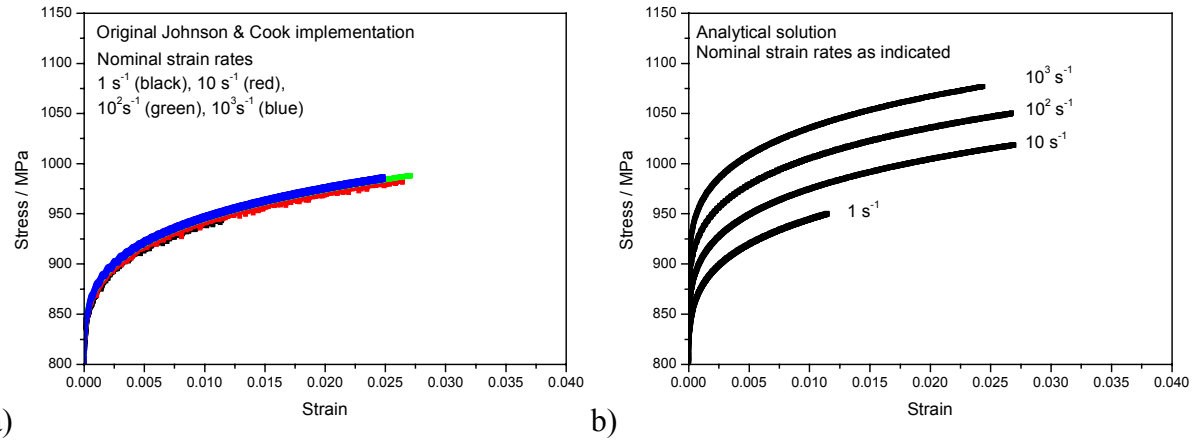

a) b)

Figure 3.6. Stress-strain curves deduced from Autodyn 2D 4.1.13 with the use of the original implementation of the Johnson and Cook material model (a) compared to the analytical solution (b) for the 4340 steel.

Due to the large deviation between the numerically calculated flow stress dependency on the strain rate and the analytically solution as discussed above a new improved implementation of

the Johnson and Cook equation in Autodyn was developed by Westerling (2001). In the standard implementation the calculation of the yield stress is based on the most recent known value of strain and strain rate and a formula according to equation 3.7 is used.

$$\sigma_{n+1} = \sigma\left(\varepsilon_n^p, \frac{\varepsilon_n^p - \varepsilon_{n-1}^p}{\Delta t}, T_n\right) \tag{3.7}$$

The user routine implemented at FOI is instead based on the plastic strain at the same time as the time at which the stress is calculated. The new formula is shown below in equation 3.8 and Westerling[3] describes this improved method in detail.

$$\sigma_{n+1} = \sigma\left(\varepsilon_{n+1}^p, \frac{\varepsilon_{n+1}^p - \varepsilon_n^p}{\Delta t}, T_n\right) \tag{3.8}$$

The improved treatment of plastic flow is implicit since ε_{n+1}^p is not known when σ_{n+1} is needed, thus a system of equations including the increment in plastic strain must be solved as discussed by Westerling (2001). In figure 3.7 the result of the new implementation is shown, together with the analytical solution. It is obvious that the agreement now is much better and the effect of strain rate enhancement is more accurate described by using the modified implementation of the Johnson and Cook equation as seen in the enlarged right figure below for a nominal strain rate of 1000 s^{-1}.

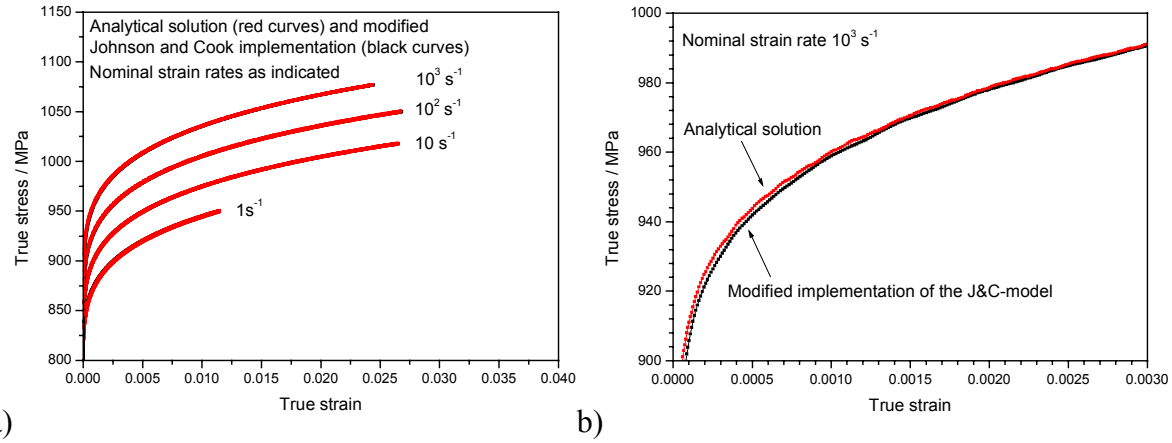

a) b)

Figure 3.7. Stress-strain curves for the 4340 steel deduced from Autodyn with the modified implementation of the Johnson and Cook material model compared to the analytical solution for strain rates 1, 10, 100, 1000 s^{-1} (a) and enlarged for strain rate 1000 s^{-1} (b).

Another useful effect of the user subroutine is that different start temperatures can easily be used. In the left part of figure 3.8 the effect of changing the start temperature from 300 to 800 K at a strain rate of 1000 s^{-1} can be seen. The right part compares the analytic solution for the flow stress from strains and strain rates deduced from Autodyn with the numerical solution. As seen the curves almost coincide and the calculations are, as before, done for the nominal strain rates 1, 10 100 and 1000 s^{-1}.

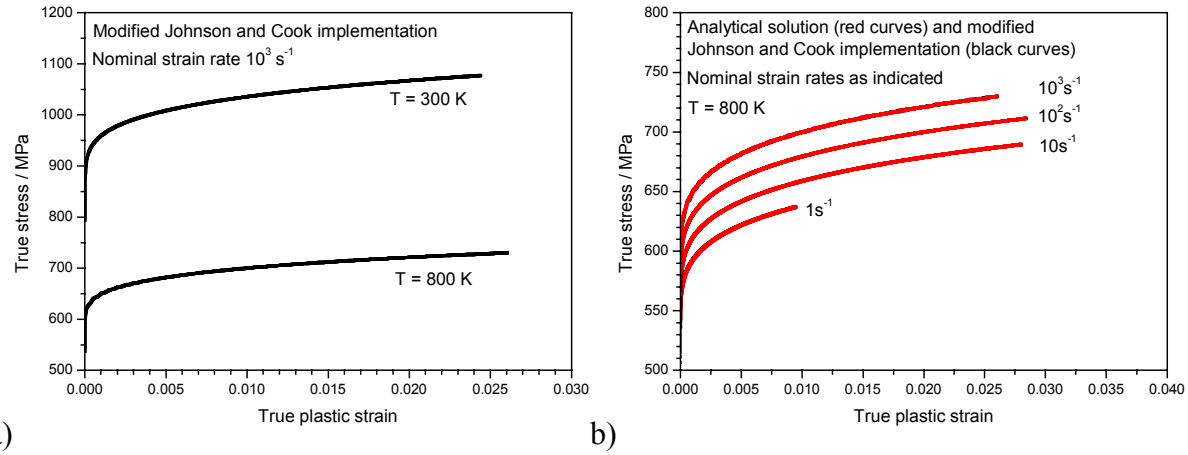

a) b)

Figure 3.8. Effect of changing the start temperature from 300 K to 800 K at a strain rate of $1000s^{-1}$(a), using the modified implementation of the J&C model. Comparison of analytical and numerical solution of the flow stress at a start temperature of 800 K, as seen the curves overlaps (b).

3.4.2. Simulation of ballistic limit for 5.56 mm AP vs. HNS target

As discussed earlier, in connection with figure 3.4, the ballistic properties of the nitrogen alloyed steel against small calibre armour piercing ammunition was experimentally determined and compared with a more traditional armour, RHA, with a similar thickness and hardness (HB≈300-320). These experiments were used for comparison with numerical simulations of the exit velocities of the AP (armour piercing) 5.56 mm projectile.
In an effort to study how the different implementations may affect a relevant problem with a high and broad range of strain rates a perforation case was used. An armour piercing projectile of tungsten carbide with the uni-axial compressive strength of approximately 5 GPa was chosen for the penetration calculations. The effect of the jacket is neglected and not taken into account in the calculations. Since the core material is stronger than the target material the projectile is assumed to behave elastic-ideal plastic and no failure model is used for the description of the armour piercing projectile. A pressure dependent yield and failure model can be used to describe the tungsten carbide in a more adequate way, and this a recommended for more complicated simulations. The pressure dependent material models consider the relative low tensile strength, high uni-axial compressive strength and very high strength during confinement for high strength material with brittle behaviour. All these stress states can occur in a projectile during the penetration phase. The physical and numerical data for the tungsten carbide is summarised in table 3.3.

Table 3.3. Estimated material properties for the tungsten carbide projectile core.

Tungsten carbide core			
Material model		**Physical properties**	
Equation of state	Linear	Density	14 g/cm^3
Strength model	Von Mieses	Bulk modulus	80 GPa
Failure model	No fail	Specific heat	134 J/kg K
Erosion	No erosion	Shear modulus	50 GPa
		Yield strength	5 GPa

The target material is described with the two different implementations of the Johnson and Cook strength model, as discussed earlier. The simulations are compared with the ballistic limit for 10.8 mm HNS determined in the earlier tests (Savage et al, 1999). The geometry of the model is shown in figure 3.9.

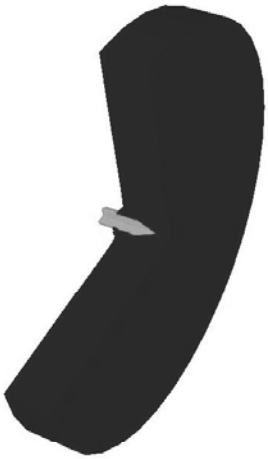

Figure 3.9. Geometry of the projectile and target during penetration with a 5.56 mm AP projectile.

Ballistic limit simulation with Autodyn 2D version 4.1.13.
Penetration simulations using the original implementation of the Johnson and Cook equation and the new user subroutine are performed and the results are compared with the experimental data discussed above. The ballistic limit was determined by using different impact velocities and calculating the exit velocity of the projectile. The input data for the numerical simulations and the results are summarised in table 3.4 and 3.5 below for the modified and original implementation respectively. The fracture criteria of 120% tensile strain are based on the result from the mechanical tests discussed above. The erosion strain is here set to 150%, while a higher value causes numerical problems due to large distortions of the mesh.

Table 3.4. Numerical models to determine the ballistic limit of 10.8 mm HNS using the modified Johnson and Cook implementation.

Characteristic parameter	**Model identity**				
	PE1002	PE1007	PE1008	PE1009	PE1005
Steel	HNS				
J&C implementation	Modified				
Strain rate enhancement	B = 0.03				
Tensile failure strain (%)	120				
Erosion strain (%)	150				
Target element size (mm)	0.2				
Projectile element size (mm)	0.4				
Gap size (mm)	0.02				
Impact velocity (m/s)	800	775	760	755	750
Exit velocity (m/s)	243	154	79	33	0
Energy error (%)	2.0	0.1	0.5	0.9	0.8

Table 3.5. Numerical simulation models to determine the ballistic limit of 10.8 mm HNS using the original Johnson and Cook implementation.

Characteristic parameter	**Model identity**					
	PE1011	PE1005	PE1012	PE1017	PE1016	PE1019
Steel	HNS					
J&C implementation	Original					
Strain rate enhancement	B = 0.03					
Tensile failure strain (%)	120					
Erosion strain (%)	150					
Target element size (mm)	0.2					
Projectile element size (mm)	0.4					
Gap size (mm)	0.02					
Impact velocity (m/s)	800	750	700	695	690	685
Exit velocity (m/s)	383	292	136	116	63	0
Energy error (%)	0.1	0.8	1.2	0.5	1.0	0.5

From the two tables above it is clear that the two implementations give very different results and the limiting velocity for penetration is close to 685 m/s for the original method while the improved calculation scheme gives about 750 m/s. Neglecting the effect of strain rate hardening, i.e. setting the parameter B in the Johnson and Cook equation to zero keeping all other data constant we calculate the exit velocities seen in table 3.6.

Table 3.6. Numerical simulation models to determine the ballistic limit of 10.8 mm HNS using the original Johnson and Cook implementation without strain rate enhancement.

Characteristic parameter	**Model identity**					
	PE1027	PE1026	PE1025	PE1024	PE1020	PE1023
Steel	HNS					
J&C implementation	Original					
Strain rate enhancement	B = 0					
Tensile failure strain (%)	120					
Erosion strain (%)	150					
Target element size (mm)	0.2					
Projectile element size (mm)	0.4					
Gap size (mm)	0.02					
Impact velocity (m/s)	800	750	700	690	680	675
Exit velocity (m/s)	417	314	170	137	75	0
Energy error (%)	0.4	0.15	0.5	0.7	0.5	0.0

As discussed earlier the strain rate parameter has a significant contribution to the deformation behaviour and the resulting penetration resistance. Excluding the strain rate effect the ballistic limit decreases from 750 m/s to about 675 m/s, while the original implementation gave 685 m/s. For comparison, the experimentally found figure is 762 m/s. The discussed results in connection with tables 3.4 to 3.6 are also visualised in figure 3.10.

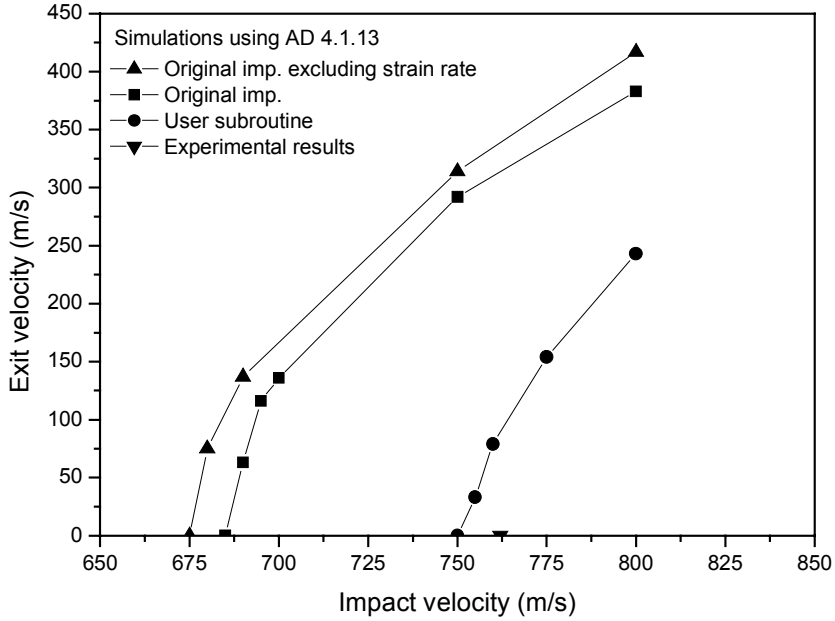

Figure 3.10. Calculated exit velocities vs. impact velocity for 5.56 mm AP penetrating a 10.8 mm thick HNS plate. The used target element size is 0.2. For comparison the experimentally found ballistic limit is also shown.

To investigate the effect of element size the mesh is decreased to 0.1 mm for both target and projectile. For these calculations the gap size is slightly decreased to 0.019 mm. For these models it was normally necessary to manually delete penetrating nodes during the simulation due to heavy distortion of the mesh. The resulting ballistic limit is decreased about 15 m/s to 735 m/s compared to the case with target and projectile cell size of 0.2 mm respectively 0.4 mm, see table 3.7. In figure 3.11 the resulting exit velocities for different element sizes as a function of impact velocities is shown together with the experimental data.

Table 3.7. Numerical simulation models to determine the ballistic limit of 10.8 mm HNS using the modified Johnson and Cook implementation and decreasing the element size to 0.1 mm.

Characteristic parameter	**Model identity**				
	PE2006	PE2007	PE2011	PE2012	PE2012
Steel	HNS				
J&C implementation	Modified				
Strain rate enhancement	0.03				
Tensile failure strain (%)	120				
Erosion strain (%)	150				
Target element size (mm)	0.1				
Projectile element size (mm)	0.1				
Gap size (mm)	0.019				
Impact velocity (m/s)	800	765	750	740	730
Exit velocity (m/s)	289	186	105	62	0
Energy error (%)	0.4	0.5	1.2	0.7	0.4

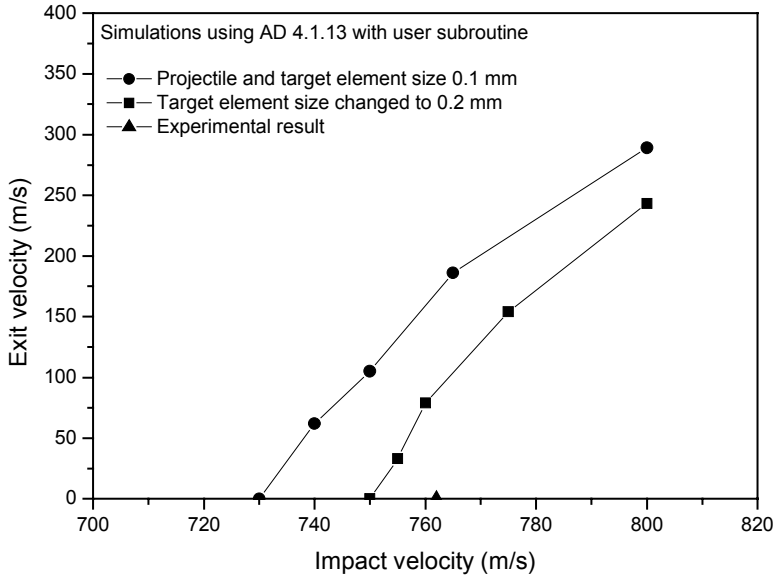

Figure 3.11. Calculated exit velocities vs. impact velocity for 5.56 mm AP penetrating a 10.8 mm thick HNS plate using the modified implementation of the JC model. For comparison the experimentally found ballistic limit is also shown.

It must however be emphasized that the numerical effects due to the choice of erosion strain are not negligible. This is also discussed in the following chapter were Autodyn version 4.2.02, is used which includes a correction for the strain rate behavior in the Johnson and Cook strength model algorithm. Further, in an effort to reduce the numerical problems associated with the Lagrange solution process and the choice of erosion strain, simulations using ALE (Arbitrary Lagrange Euler) and SPH (Smooth Particle Hydrodynamics) formulations were performed.

Ballistic limit simulation with Autodyn 2D version 4.2.02.
As mentioned earlier in the Autodyn version 4.2.02 a correction of the strain rate effect on the Johnson and Cook flow stress model is incorporated. Using this corrected version we calculate the ballistic results that can be studied in table 3.8 and 3.9 for a target element size of 0.2 mm and 0.1 mm respectively.

Table 3.8. Numerical simulation models to determine the ballistic limit of 10.8 mm HNS using the corrected implementation of the Johnson and Cook model in Autodyn 4.2.02 and a target element size of 0.2 mm.

Characteristic parameter	**Model identity**				
	PE4204	PE4202	PE4203	PE4205	PE4201
Steel	HNS				
J&C implementation	AD version 4.2.02 with corrected strain rate				
Strain rate enhancement	0.03				
Tensile failure strain (%)	120				
Erosion strain (%)	150				
Target elements	0.2 mm, Lagrange				
Projectile element size (mm)	0.4				
Gap size (mm)	0.02				
Impact velocity (m/s)	800	775	770	765	760
Exit velocity (m/s)	228	130	101	49	0
Energy error (%)	0.4	0.8	0.6	0.4	0.6

Table 3.9. Numerical simulation models to determine the ballistic limit of 10.8 mm HNS using the corrected implementation of the Johnson and Cook model in Autodyn 4.2.02 and a target element size of 0.1 mm

Characteristic parameter	**Model identity**			
	PE4213	PE4212	PE4210	PE4211
Steel	HNS			
J&C implementation	AD version 4.2.02 with corrected strain rate			
Strain rate enhancement	0.03			
Tensile failure strain (%)	120			
Erosion strain (%)	150			
Target elements	0.1 mm, Lagrange			
Projectile element size (mm)	0.1			
Gap size (mm)	0.019			
Impact velocity (m/s)	800	770	760	750
Exit velocity (m/s)	262	151	91	0
Energy error (%)	0.6	0.4	1.1	1.2

As seen, the ballistic limit decreases slightly (about 10 m/s) when the cell size is decreased to 0.1 mm. In figure 3.12 the results are visualised together with the exit velocities calculated using the subroutine developed by Westerling (2001) and Autodyn 2D version 4.1.13.

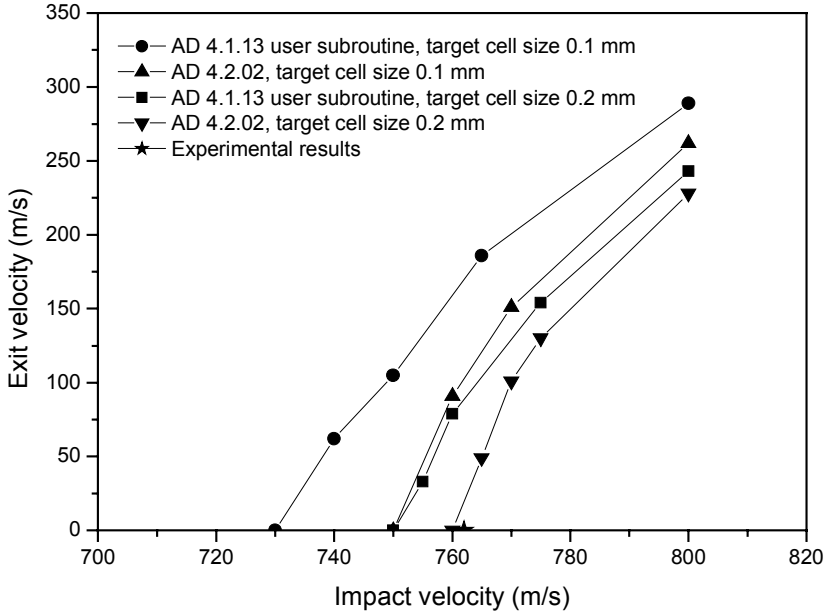

Figure 3.12. Calculated exit velocities vs. impact velocity for 5.56 mm AP penetrating a 10.8 mm thick HNS plate. Using Autodyn 4.2 and Autodyn 4.1.13 with the user implemented subroutine of the Johnson and Cook equation.

The calculated ballistic limit differs about 30 m/s using the numerical models discussed above. Further, all simulation results underestimate the ballistic limit compared to the experimental value. However, the experimental spread is ± 25 m/s in the standard for determination of the ballistic limit. The original data from the test series have not been available so the actual spread in velocity between stopped and perforating projectiles are not known. We also note that a decrease of the element size decreases the ballistic limit with about 20 m/s for the 4.1.13 calculations and 10 m/s using the 4.2.02 Autodyn version.

To illustrate the effect of different erosion strain on the resulting exit velocities a series of Lagrange simulations with Autodyn version 4.2.02 were performed without failure criteria and in table 3.10 the important parameters can be seen.

Table 3.10. Numerical simulation models to emphasise the effect of different erosion strain on the exit velocities no failure model for the target was used in the calculations.

Characteristic parameter	**Model identity**		
	PE4214[a]	**PE4215**[a]	**PE4216**
Steel	HNS		
J&C implementation	AD 4.2.02 with corrected strain rate		
Strain rate enhancement	0.03		
Tensile failure strain (%)	No fail		
Erosion strain (%)	150	140	130
Target elements	0.1 mm, Lagrange		
Projectile element size (mm)	0.1		
Gap size (mm)	0.019		
Impact velocity (m/s)	760	760	760
Exit velocity (m/s)	108	106	153
Energy error (%)	1.0	0.7	0.4

Note: [a] Some nodes manually deleted during the penetration process.

We note that for erosion strains of 140% and 150% there are no significant difference in the exit velocities (106 respectively 108 m/s) can be seen. Some nodes had to be manually deleted in order to finish the calculations for these models. Decreasing the erosion strain to 130% gives a clear increase of the exit velocity with 55 m/s to 153 m/s. Remember that by adding the tensile failure criteria resulted in a exit velocity of 91 m/s for the erosion strain of 150%, see table 3.9, model identity PE4210. Obviously, a high value of the erosion strain is desirable. However, it is not practical to use as high values as 150% due to the distortion of the elements and the accompanying numerical problems. Although, in view of the experimental results and the numerical calculations an erosion strain of 150% seems reasonable for this specific combination of target and projectile.

In an effort to reduce the problem with distorted elements the Arbitrary Lagrange Euler (ALE) approach was studied. Previously, in version 4.1 of Autodyn, only Lagrange formulation could be used in connection with the erosion algorithm. This limited the use of the ALE formulation because the remeshing of the grid is not enough to eliminate all distorted elements during penetration. In version 4.2 of Autodyn it is possible to combine ALE with erosion algorithms, and this may improve the ability to model penetration phenomena. However, a suitable value for the erosion strain is likely to differ from the figure that is used with pure Lagrange simulations. In the table 3.11 below it is seen that erosion strains of 140% and 130% decreases the exit velocity with about 25 m/s and 40 m/s.

Table 3.11. Numerical simulation models to emphasize the effect of different erosion strain on the exit velocities no failure model for the target was used in the calculations. An ALE formulation of the target is used together with erosion.

Characteristic parameter	**Model identity**			
	PE4231[a]	**PE4232**[a]	**PE4233**[a]	**PE4234**[a]
Steel	HNS			
J&C implementation	AD 4.2.02, with corrected strain rate			
Strain rate enhancement	0.03			
Tensile failure strain (%)	No fail			
Erosion strain (%)	140	130	120	110
Target elements	0.1 mm, ALE with equipotential rezoning			
Projectile element size (mm)	0.1			
Gap size (mm)	0.019			
Impact velocity (m/s)	760	760	760	760
Exit velocity (m/s)	80	115	174	202
Energy error (%)	1.6	0.8	0.6	0.2

Note: [a] Some nodes deleted during the penetration process.

One problem that occurs during the ALE simulations is the reduced time step caused by the decreased element size during the penetration. This results in a considerable increased calculation time. It also seems that the stresses in the projectile are increased for the simulations with the ALE formulation, due to larger penetration resistance. This causes plastic deformations in the nose of the tungsten carbide projectile, and rises the question of a more suitable material model for the penetrator. Both the pressure and the deviatoric stress are as high as 5 GPa in the projectile during the penetration, and thus a pressure dependent yield and failure material model for the tungsten carbide is likely to improve the simulations. The velocity contours after perforation for the ALE simulation is shown in figure 3.13a.
The small and compressed elements that cause the large decrease of the time step and a corresponding increase of the calculation time is showed in figure 3.13b.

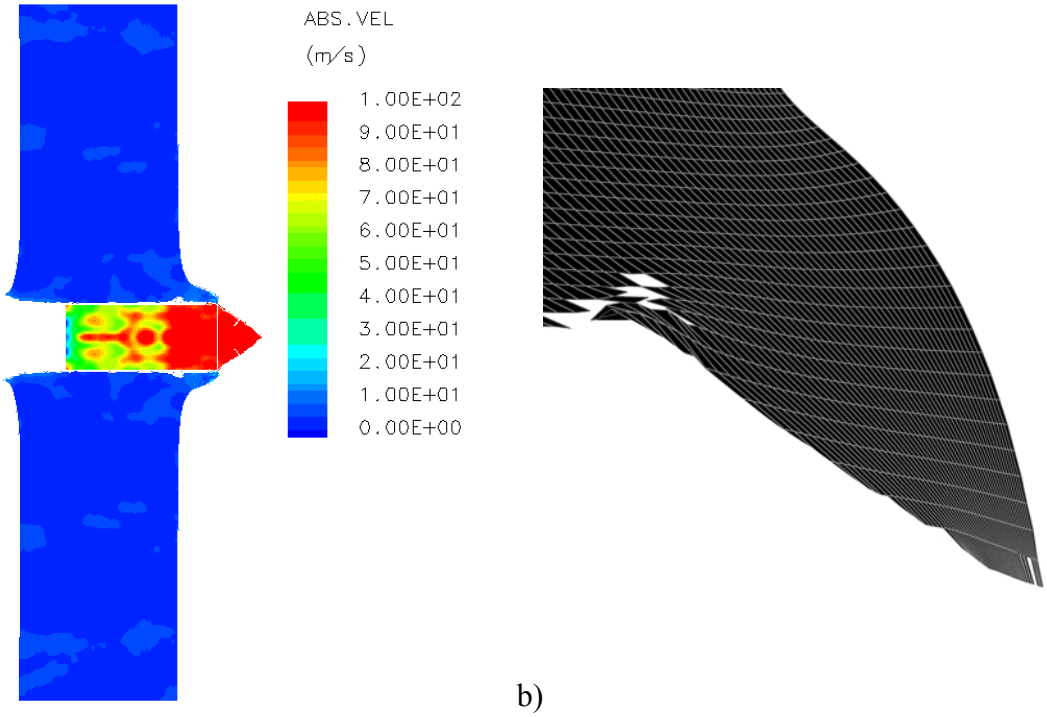

a) b)

Figure 3.13. Velocity plot after perforation of steel plate (a). Figure (b) shows the compression of the elements decreasing the time step and increasing the calculation time for model identity PE4231, see table 3.11. Figures not in scale.

A simulation with SPH (Smooth Particle Hydrodynamics) was performed for comparison with the Lagrange simulations. The advantage with SPH is that the method is meshless, and nodes with volume and mass instead represent the material. Therefore, the problem with deformed elements does not occur. The simulation was performed with the same material properties as model PE4204, except that erosion was not used. The velocities of the projectiles through the targets are shown in figure 3.14. It is seen that the decrease of velocity is similar for the two models for the first 9 mm. However, the penetration resistance for the later part of the perforation of the steel target is less for the SPH model. This is caused by a numerical failure due to the SPH formulation and results in an increased exit velocity to 283 m/s of the projectile. In figure 3.15 the different failure modes for the targets with ALE (or Lagrange) and SPH formulation is shown. The interaction between the SPH nodes will cease to exist due to the large tensile deformations that occur. This will lead to a numerical failure of the material due the lost contact between the nodes. It is possible to use a smoothing length for the SPH formulation that changes with the density of the material. This might reduce the problem of numerical failure in some models. However, the density change of the material during the perforation of the projectile is small in this case, and therefore this approach is not suitable for this kind of simulations. This type of formulation is therefore best suited for simulation of non-perforating projectiles, or penetration in brittle materials i.e. concrete and ceramics.

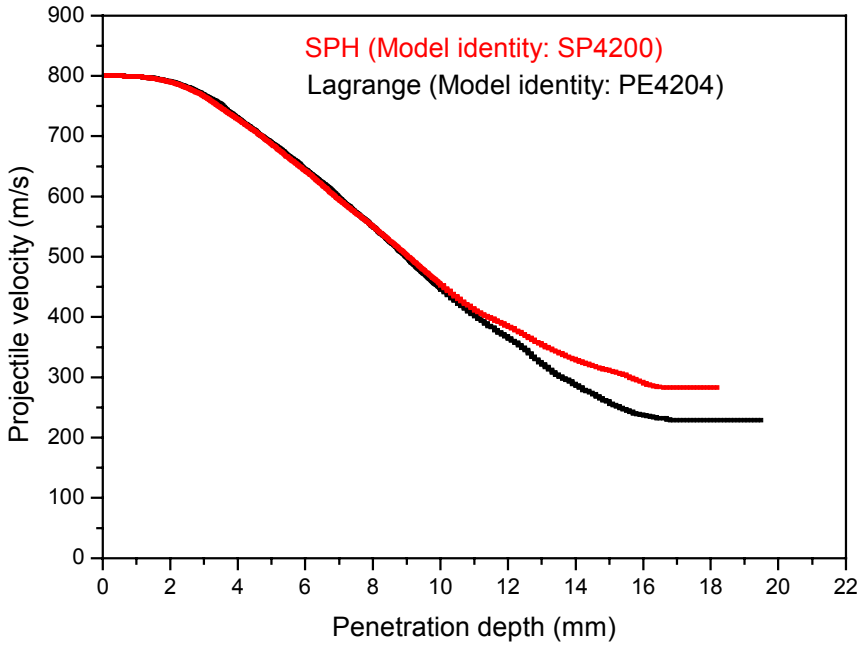

Figure 3.14. Velocity vs. penetration for a Lagrange (PE4200) and a SPH (SP4204) model. The exit velocity is changed from 228 to 283 m/s using the Lagrange respectively the SPH formulations.

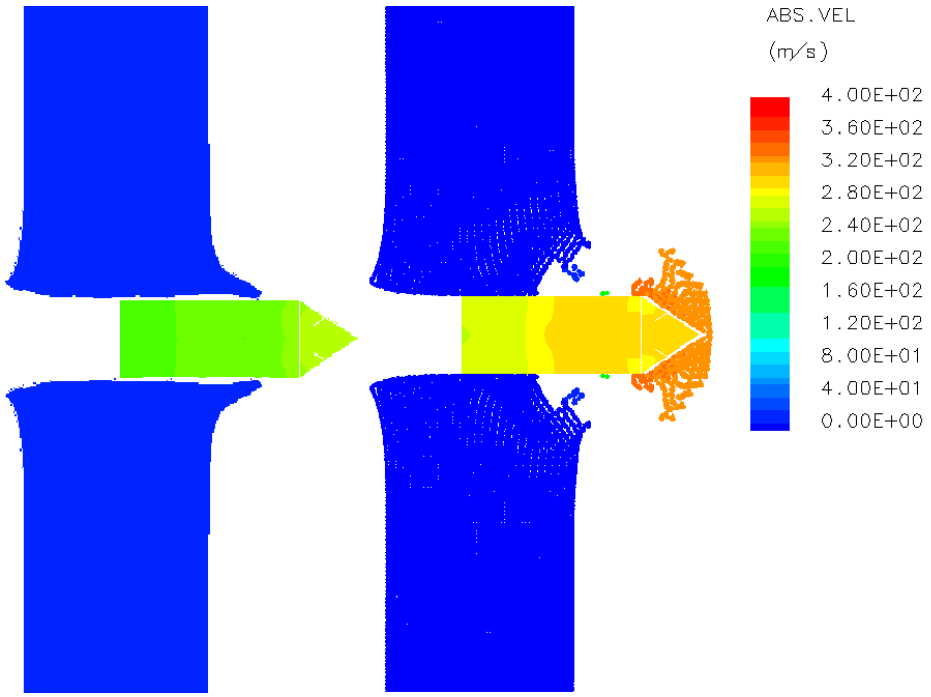

Figure 3.15. Velocity after perforation of steel target using a Lagrange formulation (left, model identity PE4204) and a SPH model (right, model identity SP4200). As seen, different failure modes occur. Figures not in scale.

4. MODELLING OF CONCRETE PERFORATION

This chapter describes work done with an advanced material model for concrete, the used material model is the RHT concrete model developed at EMI (Riedel, 1998 and 2000). The version of the material model that is used for the work reported here is implemented as a standard model in Autodyn version 4.2 or higher. The study was performed with Autodyn 2D version 4.2.00v (β-release). The results from a benchmark test series from 1999 with 152 mm ogive nosed projectiles are briefly described and also used as a reference case for the simulations. Comparisons are made between simulations performed with Lagrange, Euler and SPH formulation, and the strengths as well as weaknesses of the different formulations are discussed.

4.1. The RHT concrete model

The RHT model is implemented in the general release of Autodyn 4.2. This report describes the general release version of the RHT concrete model. The first version of RHT concrete model is described in Riedel (1998), and also examples of material parameters for concrete is given in this reference. A later version of the model is presented in the Ph. D. thesis by W. Riedel (2000), this version is the one implemented in Autodyn with some modifications. Earlier simulations with the model are further presented in Riedel (1999), Ågårdh and Hansson (1999), and Hansson and Ågårdh (2000). At the 10th ISIEMS Svinsås et. al. (2001) presented simulations of the benchmark tests with a modified RHT model for Autodyn 2D version 4.1.13. The simulations in this report are performed with the RHT model as implemented in Autodyn 2D version 4.2.00v (β-version). Minor changes of the code are likely to occur until the general release.

The concrete model used different strength surfaces to define the elastic limit, failure surface and residual strength surfaces. A principle figure of the elastic limit and failure surfaces is shown in figure 4.1. The pressure dependence of the failure strength is given on a normalised form according to eq. (4.1). The reduction of the failure strength between the compression and the tension meridians is given by eq. (4.2) and (4.3). The model also accounts for the loading rate according to eq. (4.4). There is also an option in the model to use a cap on the elastic strength surface. The various effects are given as factors according to eq. (4.5). where f = 0 defines points on the failure surface. Equations and diagrams below from Riedel (2000).

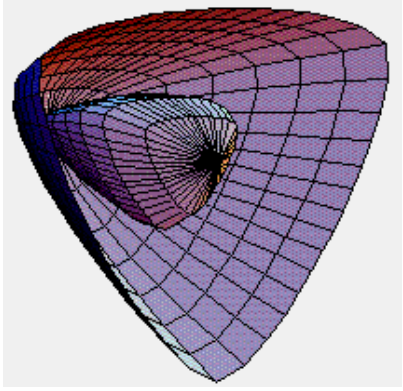

Figure 4.1. Elastic strength surface with cap and failure surface for the RHT model, from Riedel (1998).

$$Y^*_{TXC(P)} = \frac{Y_{TXC(p)}}{f'_c} = A_{fail} \cdot \left[p^* - \left(p^*_{spall} F_{Rate}\right)\right]^{N_{fail}} \tag{4.1}$$

$$R_3(\theta) = \frac{2\left(1-Q_2^2\right)\cos\theta + \left(2Q_2 - 1\right)\left[4\left(1-Q_2^2\right)\cos^2\theta + 5Q_2^2 - 4Q_2\right]^{\frac{1}{2}}}{4\left(1-Q_2^2\right)\cos^2\theta + \left(1-2Q_2\right)^2} \tag{4.2}$$

$$Q_2 = Q_{2,o} + BQ \cdot p^* \ with\ 0.5 \le Q_2 \le 1\ and\ BQ = 0.0105 \tag{4.3}$$

$$F_{RATE(\dot{\varepsilon})} = \begin{cases} \left(\dfrac{\dot{\varepsilon}}{\dot{\varepsilon}_0}\right)^{\alpha} & for\ P > f_c/3\ ,\ with \dot{\varepsilon}_0 = 30 \times 10^{-6}\ s^{-1} \\ \left(\dfrac{\dot{\varepsilon}}{\dot{\varepsilon}_0}\right)^{\delta} & for\ P < f_c/3\ ,\ with \dot{\varepsilon}_0 = 3 \times 10^{-6}\ s^{-1} \end{cases} \tag{4.4}$$

$$f(p, \sigma_{eq}, \theta, \dot{\varepsilon}) = \sigma_{eq} - Y_{TXC(P)} F_{CAP(P)} R_{3(\theta)} F_{RATE\ (\dot{\varepsilon})} \tag{4.5}$$

The elastic limiting surface is determined through the parameters PREFACT, COMPRAT and TENSRAT. PREFACT defines the ratio between the original shear modulus and the corresponding value after the elastic limit has been passed. COMPRAT defines the ratio between the elastic compressive limit and the compressive strength limit and TENSRAT corresponding ratio in tension.

The damage in the material grows after the stress point passes the failure surface according to eq. (4.6) and (4.7). The residual strength of the fully damaged concrete is calculated from eq. (4.8). The strength is then interpolated from the strength values for the undamaged material (D=0) and the completely damaged material (D=1) according to eq. (4.9), depending on the accumulated damage.

$$D = \sum \frac{\Delta \varepsilon_p}{\varepsilon_p^{failure}} \tag{4.6}$$

$$\varepsilon_p^{failure} = D_1\left(P* - P*_{spall}\right)^{D_2} \tag{4.7}$$

$$Y^*_{residual} = B \cdot \left(P^*\right)^M \tag{4.8}$$

$$Y^*_{fractured} = \left(1 - D\right) Y^*_{failure} + D \cdot Y^*_{residual} \tag{4.9}$$

The Equation of State (EOS) is based on the "P-α-model". Explanation is published by Herrman (1969) and is also described in the Autodyn theory manual (2000). The behaviour of the solid material is given by eq. (4.10a-b), while the porous compaction is given by eq. (4.11). The compaction, α(p,e), gives the behaviour of the porous material in the pressure range of pore collapse (p_{crush}) and full compaction (p_{look}).

$$P = A_1\mu + A_2\mu^2 + A_3\mu^3 \quad with \quad \mu = \frac{\rho}{\rho_0} - 1 \geq 0 \tag{4.10a}$$

$$P = T_1\mu + T_2\mu^2 \quad with \quad \mu = \frac{\rho}{\rho_0} - 1 < 0 \tag{4.10b}$$

$$P = f(\rho, e) \overset{porous}{\rightarrow} P = f(\rho\alpha, e) \quad with \quad \alpha = 1 + (\alpha_{init} - 1)\left[\frac{P_{lock} - P}{P_{lock} - P_{crush}}\right]^n \tag{4.11}$$

The parameters for the RHT concrete model are compiled in table 4.1.

Table 4.1. Material parameters for the RHT concrete model and P-α equation of state.

Parameter	Description
ρ_0	Initial density
ρ_{porous}	Porous density
c_{porous}	Porous sound speed
p_{crush}	Initial compaction pressure
p_{lock}	Solid compaction pressure
n	Compaction exponent n
Solid EOS	Type of solid EOS, i.e. Polynomial
ρ_{solid}	Reference density for solid EOS
A_1	Parameter A_1 for polynomial EOS, for compression.
A_2	Parameter A_2 for polynomial EOS, for compression.
A_3	Parameter A_3 for polynomial EOS, for compression.
B_1	Parameter B_1 for polynomial EOS
B_2	Parameter B_2 for polynomial EOS
T_1	Parameter T_1 for polynomial EOS, for expansion.
T_2	Parameter T_2 for polynomial EOS, for expansion.
T_{ref}	Reference temperature
c_v	Specific heat
G	Shear modulus
f'_c	Compressive strength
f_t/f_c	Tensile compressive strength ratio
f_s/f_c	Shear compressive strength ratio
A_{fail}	Failure surface parameter A, initial slope of failure surface
N_{fail}	Failure surface exponent N, pressure dependence for failure surface
Q_2	Tensile compression meridian ratio
BQ	Brittle to ductile transition
$\frac{G_{elastic}}{G_{elastic-plastic}}$	Ratio between elastic shear modulus and elastic-plastic shear modulus. (PREFACT)
$f_{t,\,elastic}/f_t$	Ratio between elastic surface and failure surface for tension (TENSRAT)
$f_{c,\,elastic}/f_c$	Ratio between elastic surface and failure surface for compression (COMPRAT)
Cap option	Use cap on elastic surface
B	Residual strength constant B, initial slope of residual surface
M	Residual strength exponent M, pressure dependence for residual surface
α	Compressive strain rate exponent a
δ	Tensile strain rate exponent d
D_1	Damage constant D_1
D_2	Damage exponent D_2
$\varepsilon_{fail,\,min}$	Minimum strain to failure
$G_{residual}/G_{elastic}$	Residual shear modulus fraction (SHRATD)
Tensile failure model	Use of "Hydro tensile limit" or "Principal stress" for tensile failure description
P_{min}	Hydro tensile limit failure
$\sigma_{tensile\ failure}$	Tensile failure stress for "Principal stress" failure condition
$\tau_{maximum}$	Shear failure stress for "Principal stress" failure condition
Gf	Crack softening for "Principal stress" failure condition

4.2. Benchmark tests with 152 mm projectiles

In October 1999 a series of benchmark tests were conducted. These tests were a co-operation project with DERA, FOA, FFI and TNO as participants. The purpose with the benchmark tests was to obtain reliable data for numerical simulations, and be able to test the available numerical methods and material models for simulation of penetration in concrete.

4.2.1. Material properties

The concrete for the benchmark test series was tested with standard methods to obtain E-modulus, cube strength and splitting strength. The behaviour of the concrete during tri-axial loading was tested with passive confinement of the concrete with GREAC cells by FFI and Imperial College. The properties of concrete targets are given in table 4.2, and in figures 4.2 and 4.3.

Table 4.2. Properties of the concrete targets.

Target/concrete properties	Value
Diameter	2.40 m
Length	0.75 m
Compressive uni-axial cube strength*	103 ± 2 MPa
Compressive uni-axial cylinder strength**	92 ± 2 MPa
Tensile splitting strength*	6.5 ± 0.2 MPa
Tensile splitting strength**	5.9 ± 0.6 MPa
Initial E-modulus** (E_0)	44.0 ± 0.5 GPa
E_c **	44.5 ± 0.9 GPa

Note: *: Determined on cubes with 150 mm side.
**: Determined on ∅100×200 mm cylinders.

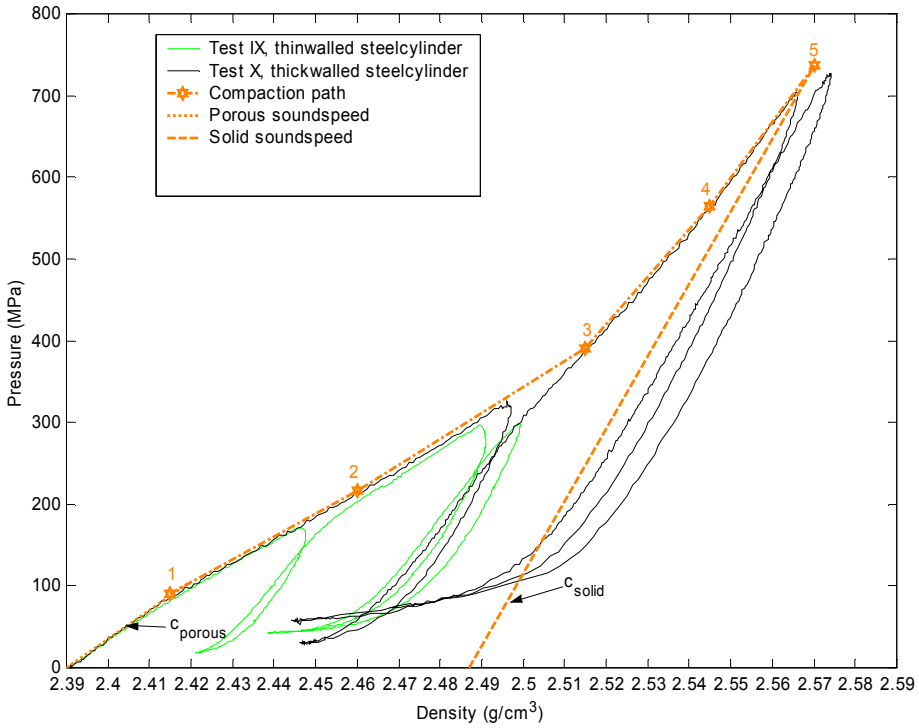

Figure 4.2. Pressure vs. density for samples tested in a GREAC cell at FFI.

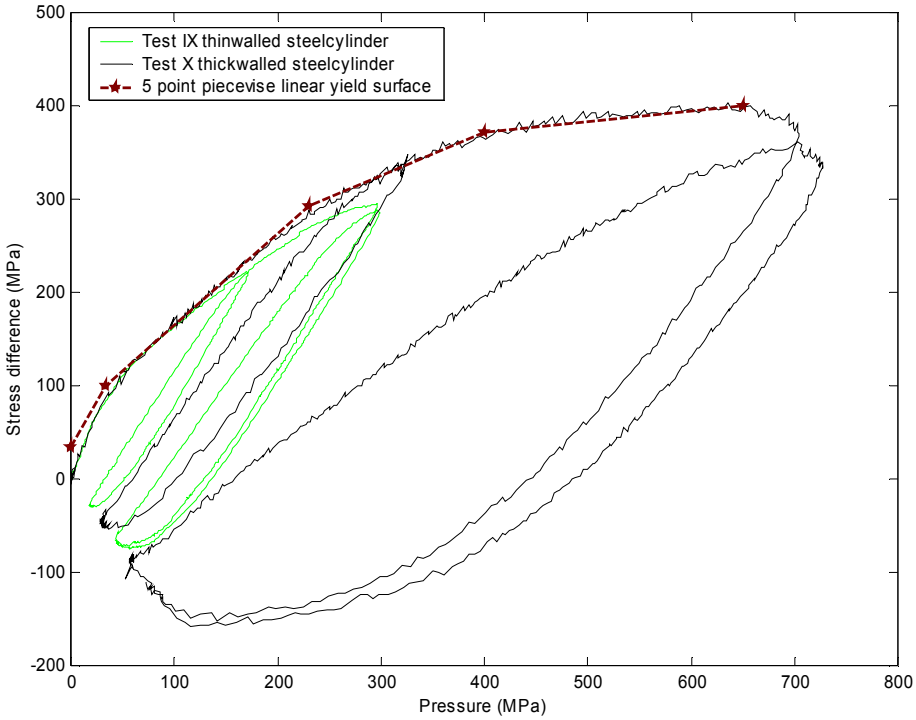

Figure 4.3. Stress difference vs. pressure for samples tested in a GREAC cell at FFI.

4.2.2. Benchmark penetration tests

The benchmark tests were performed with an instrumented spinning projectile with 152 mm diameter, see figure 4.4 and table 4.3. Three tests were conducted with unreinforced concrete with the approximate cube strength of 100 MPa. Two of the projectiles were equipped with accelerometers to determine the deceleration during the perforation in the target. The exit velocity of the projectiles was determined with a high speed video camera for comparison with data from accelerometer recordings and Doppler radar measurements. Two of the targets were equipped with pressure transducers, which were mounted 30 cm from the back face of the targets. The impact and exit velocities of the projectiles are given in table 4.3. A target before impact is shown in figure 4.4, and a target after perforation is shown in figure 4.5.

Numerical integration of the accelerometer signal from instrument pack in the projectile underestimated the velocity of the projectile in comparison with velocity measurement from Doppler radar and exit velocity determined by high speed video. The radar measurements seem to have registered the velocity during the major part of the projectile deceleration in the target. Also the lower projectile exit velocity for test 25 in comparison with test 24 is shown in the radar measurements. The data from the accelerometer and radar are shown in figures 4.6 to 4.8.

Table 4.3. Benchmark test data.

	Test 23	Test 24	Test 25	Mean value
Diameter	152 mm			
Length	552 mm			
Ogive radius	380 mm			
Nose length	228 mm			
Total mass	46.2 ±0.1 kg			
Mass of case	38.8 kg			
Type of projectile	Dummy	Instrumented*	Instrumented	----
Impact velocity	460.0 ±0.5 m/s	455.5 ±0.2 m/s	458.8 ±0.2 m/s	458.1 ±0.2 m/s
Exit velocity**	183 ±6 m/s	204 ±4 m/s	181 ±4 m/s	190 ±14 m/s

Note: * Instrumentation pack not recovered after test. **: Determined from high speed video.

Figure 4.4. 152 mm projectile and target mounting for benchmark tests.

Figure 4.5. Target after perforation for test no. 24, front face to the left

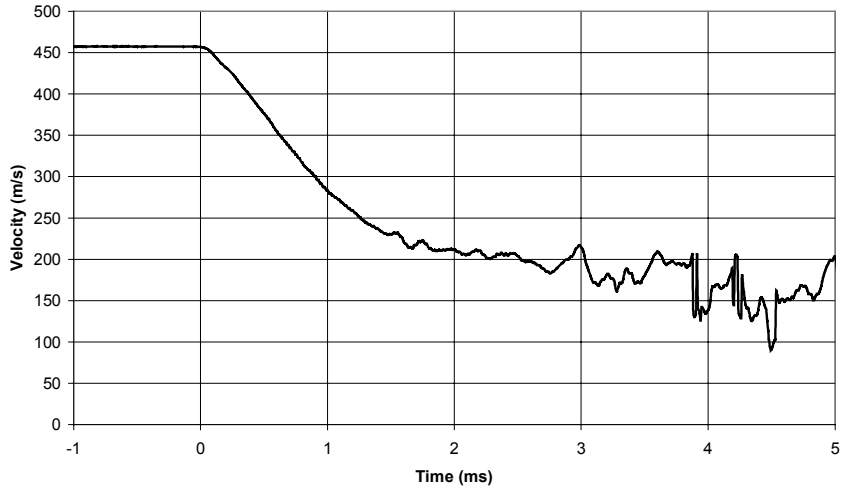

Figure. 4.6. Mean values of radar measurements for tests 24 and 25.

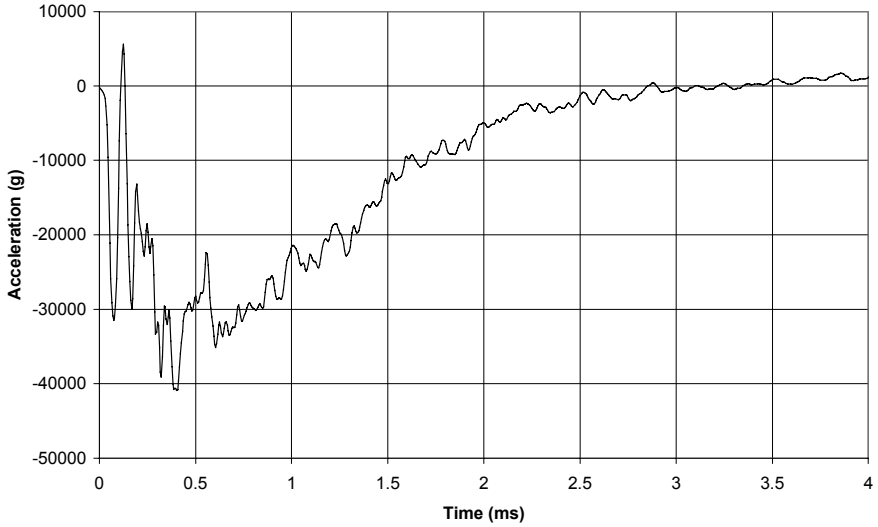

Figure 4.7. Moving average of 9 points for acceleration registration from projectile for test no. 25.

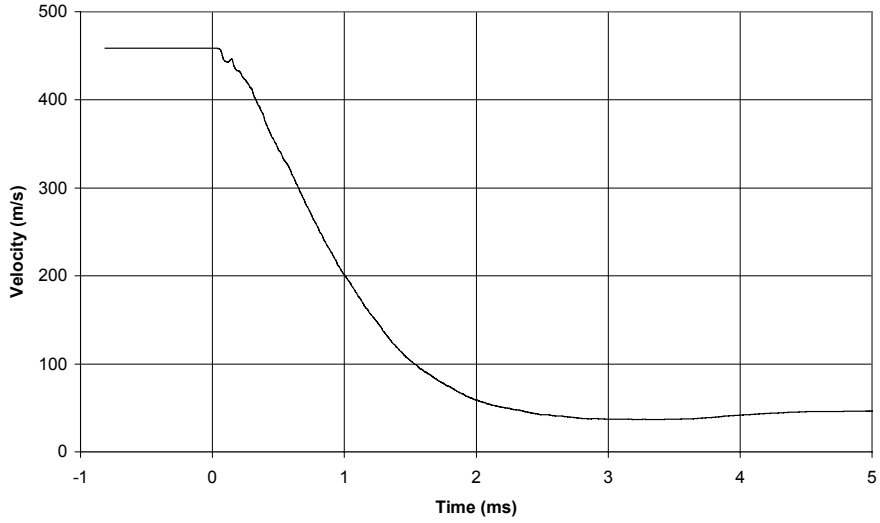

Figure 4.8. Velocity of projectile obtained by integration of acceleration data from projectile for test no. 25.

4.3. Numerical simulation of benchmark tests

4.3.1. Material parameters used for simulation with RHT model

The chosen values of the material parameters for the RHT model were based on the material test described in previous chapter. The strength from the cylinder test was used as uni-axial compressive strength for the simulations. The uni-axial tensile strength is normally 80% to 90% of the splitting strength. Therefore, the tensile strength was chosen as 5.2 MPa. This is approximate 80% of the splitting strength for 150 mm cubes and 90% of the splitting strength for ∅100 mm cylinders. The elastic area for high performance concrete is larger than for normal strength concrete. The elastic part of the uni-axial compression strength was assumed to correspond to 0.75 of the failure stress (COMPRAT). These assumptions were based on the stress-strain relationship from uni-axial stress tests. The ratio between elastic and failure tension strength is greater than the ratio between elastic and failure compression strength. According to this the factor TENSRAT was chosen to be 0.8. The ratio between elastic and elastic-plastic shear modulus was chosen to 2, this is a normal value for this material model. The initial bulk and shear modulus was based on the measured initial Young's modulus. Based on these assumptions the elastic shear modulus was chosen to be 18.0 GPa and Poisson's ratio 0.18, which gives a bulk modulus of 21.5 GPa and initial Young's modulus of 42.5 GPa. The parameters that have greatest uncertainty are the ratio between shear strength and uni-axial compression strength, and the definition of the residual strength surface. Strain rate enhancement for the concrete is based on comparison with similar concrete types. The values for the parameters to the RHT model are given in table 4.4. The failure surfaces are also given in figure 4.9.

The pressure vs. density is based on measurement data from FFI shown earlier in figure 4.2. This ratio between pressure and density, equation of state, is determined under static loading. However, it is known that the relationship between pressure and density is influenced by the loading rate for the material. It has been shown that a high strain rate results in greater pressure for the same compaction of the concrete. According to this it is difficult to determine a correct EOS to be used for the concrete subjected to high strain rate loading from static tests. The reason to use the data from the static tests for the simulations is that there are no dynamic data available. There are two options that can be used for the tensile failure together with the RHT model, and these are "Principal stress" and "Hydro tensile limit". Of these the hydro tensile limit tensile failure condition was used for the simulations. Further data are given in Hansson (2001).

Table 4.4. Used material parameters for the RHT concrete model, except when other values are specified.

Parameter	Values	Parameter	Values
G	18.0 GPa	Cap on elastic surface	Yes
f'_c	92.0 MPa	B	1.3
F_t/F_c	0.057	M	0.65
F_s/F_c	0.30	α	0.010
A	1.9	δ	0.013
N	0.6	D_1	0.04
Q_2	0.6805	D_2	1
BQ	0.0105	EFMIN	0.01
PREFACT	2	SHRATD	0.13
TENSRAT	0.80	Tensile failure model	Hydro tensile limit
COMPRAT	0.75		

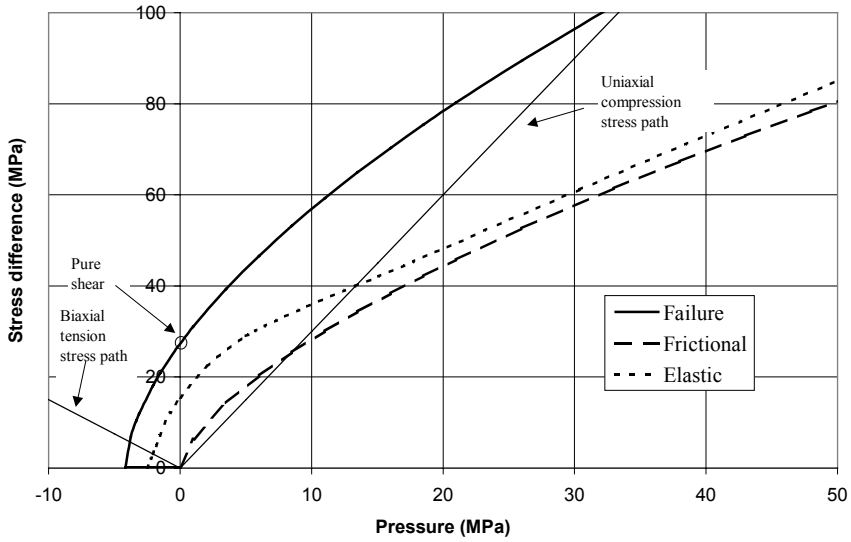

Figure 4.9. Stress difference vs. pressure for simulations.

4.3.2. Numerical simulation for verification of concrete material model

Numerical simulations were performed to make a first attempt to study the behaviour of the RHT concrete model for Autodyn version 4.2. However, further studies are needed for the general release of the program code.

A model with a cylindrical geometry was used to study the response of the material model. Rotational symmetry was used for the cylinder with 50 mm diameter and a length to diameter ratio of 2. No friction is considered for the top and bottom surfaces. The element size in the models is 2.5 mm, with geometry of model shown in figure 4.10. For further data on the simulations see Hansson (2001).

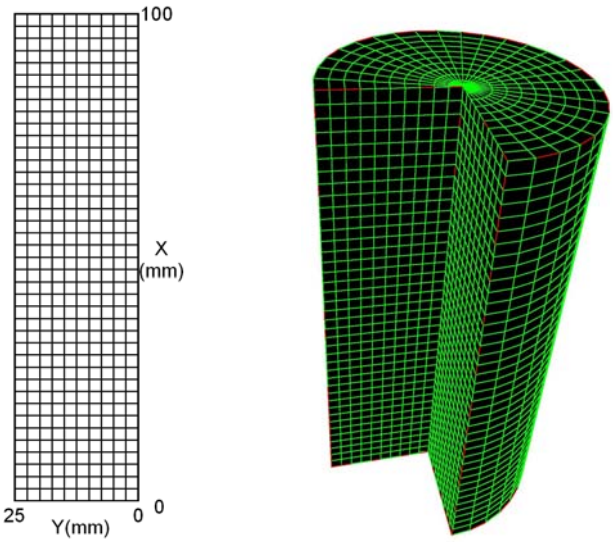

Figure 4.10. Geometry of rotation symmetric model with 2.5 mm element sides. The model is rotated 270° for the plot to the right, with the x-axis as the centre of revolution.

Hydrostatic compression

The behaviour of the models were tested for hydrostatic pressure loading, with the obtained pressure vs. density relationships shown in figures 4.11.

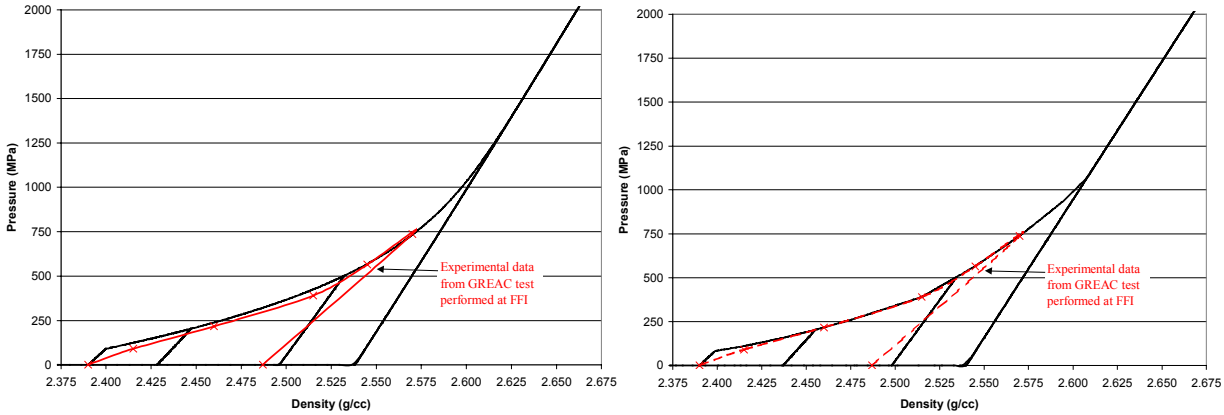

Figure 4.11. Hydrostatic loading and unloading path for a concrete cylinder, with the use of P-α (left) and porous EOS.

Uni-axial compression test

Uni-axial test were simulated to determine the models response at different loading rates, and with the use of different strain rate sensitivity for the material model. The obtained strain rate effects are shown in figure 4.12. The calculated relationship between deformation and stress are given in figure 4.13 where the dependence of strain rate is shown.

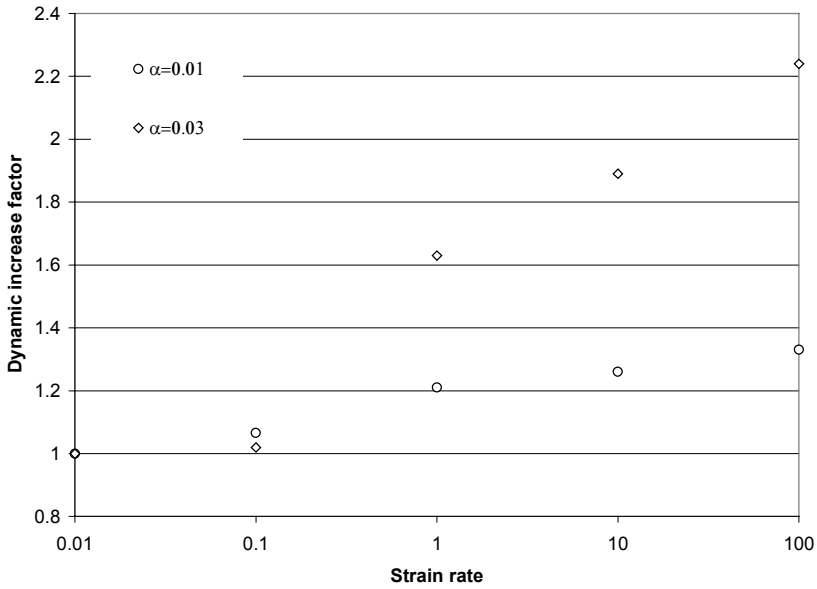

Figure 4.12. Dynamic increase factor for uni-axial compressive stress with pressure effects included. Normal values for α are 0.01 for HPC and 0.03 for normal strength concrete.

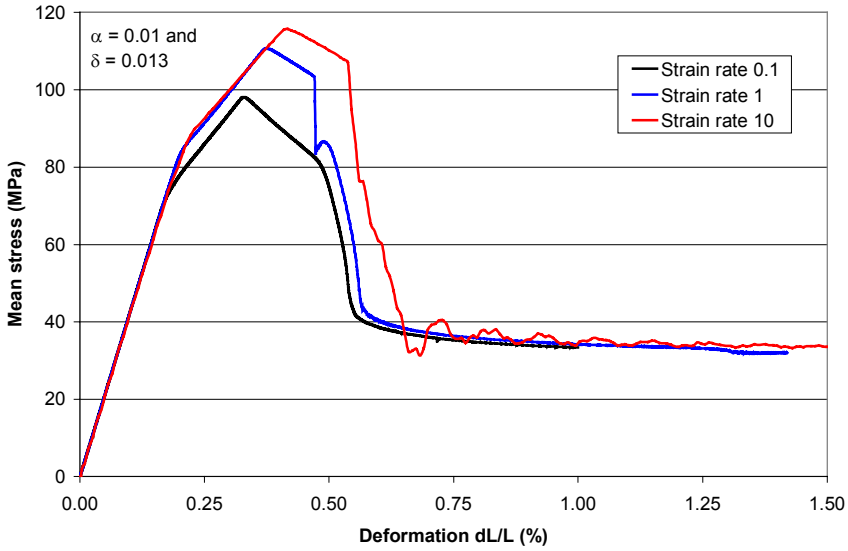

Figure 4.13. Average axial stress vs. axial deformation for different strain rates and α equal to 0.01.

Uni-axial strain (compression)

Simulations of uni-axial strain deformation for compression were performed. This loading condition are close to the one obtained for the GREAC cell. The axial stress vs. pressure for a model without strain rate enhancement is given in figure 4.14, and the stress difference vs. pressure for the same model is given in figure 4.15.

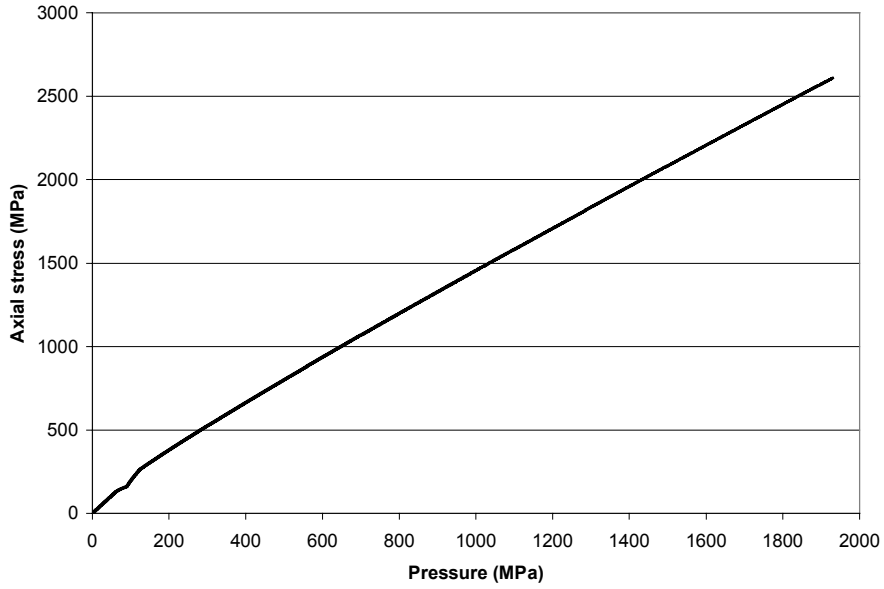

Figure 4.14. Axial stress vs. pressure for uni-axial compressive strain loading for a model without strain rate enhancement (α=0).

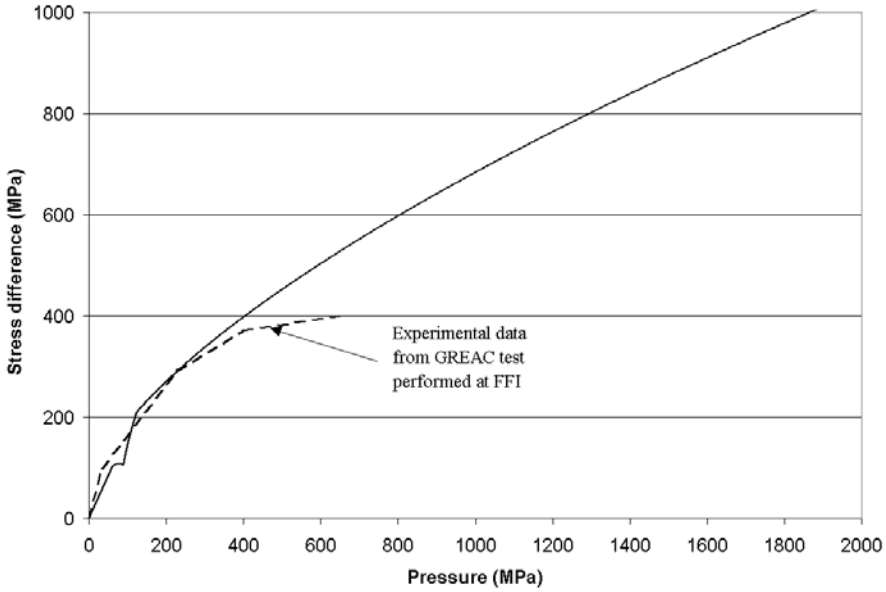

Figure 4.15. Stress difference between axial and radial stress vs. pressure for uni-axial compressive strain loading, for a model without strain rate enhancement (α=0).

Uni-axial tension test

Uni-axial tension loading were also used to study the behaviour of the material model. Local damage were induced in the cylinder models, which results in a decreased average stress for the models. Therefore, the cylinder geometry was complemented with one element models to study the strain-stress relationship for tension. However, both type of models were sensitive to the chosen value for the damping for the simulation, which seems to be caused by the transition from elastic yield surface to the failure surface in the RHT material model. The tensile behaviour of the material model needs to be improved to describe the tensile failure of the concrete. This is an area in which EMI is working to improve the material model.

4.3.3. Numerical simulation of penetration with the RHT model

The numerical simulations of the benchmark test were performed with Autodyn 2D version 4.2.00v with the RHT material model. Simulations were performed both with Lagrange Euler and SPH formulation for comparison. 2D axial symmetry was used for the models. Material parameters for the models are mainly from previous chapter 4.1. However, some material properties are varied to study the influence on the exit velocity. The geometry for the penetration simulations is shown in figure 4.16 below.

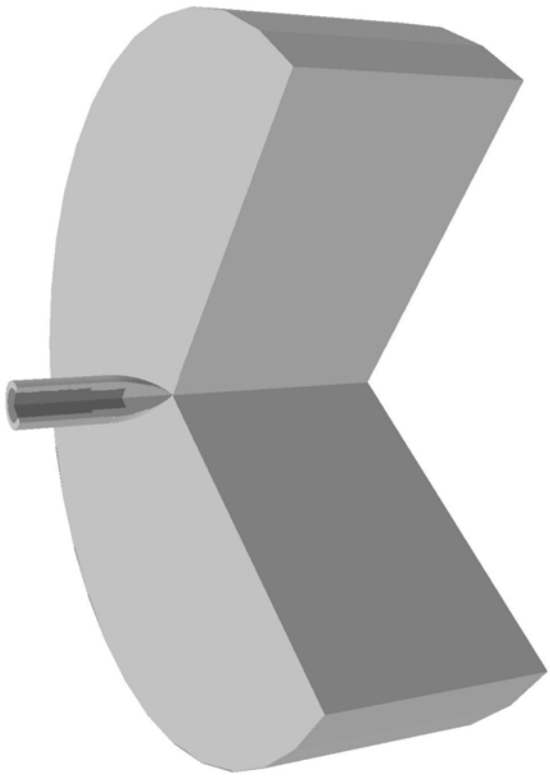

Figure 4.16. Geometry for the simulations is shown with 270° rotation of the model for visualisation.

Numerical simulation with Lagrange formulation for the target

When a Lagrange formulation is used to represent a target during penetration it is necessary to use numerical erosion to eliminate heavily distorted elements. However, this causes material to be removed from the mesh and thereby reduced mass and confinement. This type of model might give a reasonable result for materials that do not have a pressure dependent yield stress, i.e. steel. However, concrete, rock, soil and ceramics have a pressure dependent yield stress and failure type, and the calculation results are therefore likely to be influenced by the use of numerical erosion together with the Lagrange formulation for penetration simulation. The parameters for the Lagrange models are shown in table 4.5.

Table 4.5. Model properties for simulations with Lagrange elements, except when other values are specified.

Model	**B99008-38**	**B99055-57**
Element type	Lagrange target and projectile formulation	
Size of target subgrid	0.75×1.2 m	
Element size in target	10×10 mm	5×5 mm for r<500 mm
No. of elements in target	75×120=9,000	150×180=27,000
Element size in projectile	15×10 mm	
No. of elements in projectile	21×7=147	
Projectile mass and velocity	46.2 kg, 459 m/s	
Equation of state	P-α	
f_c	92 MPa	
$f_{t,\ elastic}/f_t$	0.80	
Failure surface parameter A	1.90	
Failure surface exponent N	0.60	
Residual strength constant B	1.60	
Residual strength exponent M	0.61	
f_s/f_c	0.30	
D_1	0.08	
D_2	1.0	
EFMIN	0.05	
α	0.010	
δ	0.013	
Friction coefficient	No friction	
Gap size for interaction	1 mm	0.5 mm
Erosion strain	150%	
Static damping	0	
Linear viscosity	0.2	

Note: * Elements graded in radial direction to 5×13 mm at boundary.

Several parameters influence the results and interact with the erosion algorithm for a model with a Lagrange formulation for the target, i.e. the chosen gap size, coefficient of friction and element size. The simulations with values greater than 150% for the erosion strain resulted in large energy errors. This result appeared both for the 5 and 10 mm element sizes, see tables 4.xx and 4.xx. The energy errors were caused by local errors in the area of contact between the projectile and target. This phenomena is likely to be caused by the heavily distorted elements in the contact zone, see figure 4.20. These energy errors decreased when the element size in the target was reduced to 5 mm. As expected it was also shown that the erosion strain influenced the calculation results when Lagrange formulation was used for the target. A low value on the erosion strain results in an increased exit velocity, and high values of the erosion strain resulted in an increased energy error for the calculation. Therefore, an erosion strain of 150% was chosen for the simulation with the Lagrange formulation.

The friction between target and projectile was also varied, with no significant change for the exit velocity. However, there is a significant increase for the energy error when friction is used between the target and projectile. The increased friction is likely to increase the shear strain in the target, and thereby distort the elements to a greater degree. The friction was therefore neglected for the major part of the Lagrange simulations.

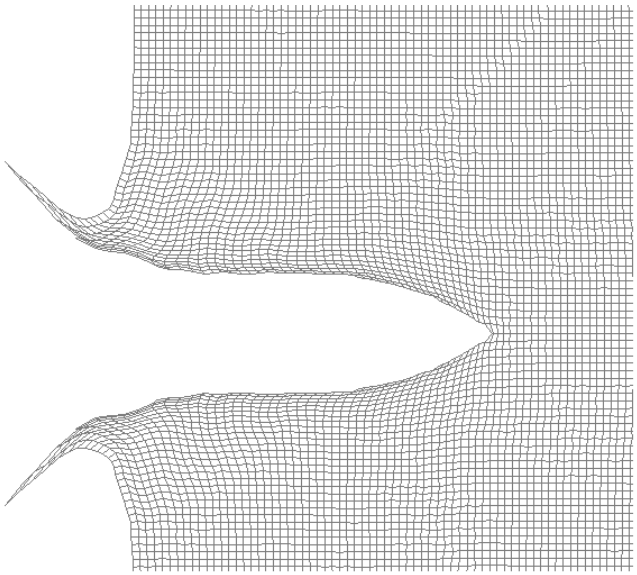

Figure 4.17. Distorted target grid during penetration for a model with 10 mm Lagrange elements.

A limited study of the influence from the chosen material parameters was also conducted, with parameters changed to general values for the RHT model. The major influence on the exit velocity was from shear strength (f_s/f_c), residual strength surface (B, M) and damage parameters (D_1, D_2, EFMIN). The combination of changed damage parameters and residual strength surface will cause a major decrease of the exit velocity of the projectile. Some results from the simulations are shown in table 4.6.

The exit velocities for the simulations B99035 and B99036 with decreased damage propagation are close to the one obtained in the experiments. If these model parameters also result in an acceptable accuracy for other similar experiments need to be evaluated in the future. However, the residual strength and damage parameters are the most difficult to determine for the material model.

Table 4.6. Lagrange models with 10 mm element size with variation of damage parameters and residual strength.

Model	**B99008**	**B99035**	**B99036**	**B99038**
Residual strength constant B	1.60	1.90	1.6	
Residual strength exponent M	0.61	0.60	0.61	
D_1	0.04	0.08		0.04
EFMIN	0.01	0.05		
Friction	No friction			
Exit velocity	247 m/s	194 m/s	189 m/s	212 m/s
Energy error	0.9 %	1.0 %	1.0 %	1.1 %

The influence from the size of the elements in the model was checked with simulations with 5 mm Lagrange elements. The model with 5 mm elements offers less resistance for the projectile compared with the model with 10 mm element size and the same model properties. To obtain an exit velocity comparable to the experiments it is also necessary to introduce friction between target and projectile. It seems difficult to determine if and how much the friction accounts for the deceleration of the projectile in the real case. If these model parameters also result in an acceptable accuracy for other similar experiments need to be evaluated in the future. As mentioned before the residual strength, and damage parameters are the parameters that are difficult to determine. Also the friction coefficient are an uncertain parameter for this type of simulations. It was also mentioned before that the induced friction causes greater shear deformation to the target elements close to the contact surface, and thereby is likely to increase the erosion of target. The parameters of the models are compiled in table 4.7. In figure 4.18 the measured velocity from the radar are compared with the calculated velocity for model B99057.

Table 4.7. Lagrange models with 5 mm element size, different residual strength and damage parameters.

Model	B99055	B99056	B99057
Friction coefficient	No friction		0.05
Residual strength constant B	1.60		
Residual strength exponent M	0.61		
D_1	0.04	0.08	
EFMIN	0.01	0.05	
Exit velocity	269 m/s	237 m/s	207 m/s
Energy error	0.5 %	0.6 %	8.6 %

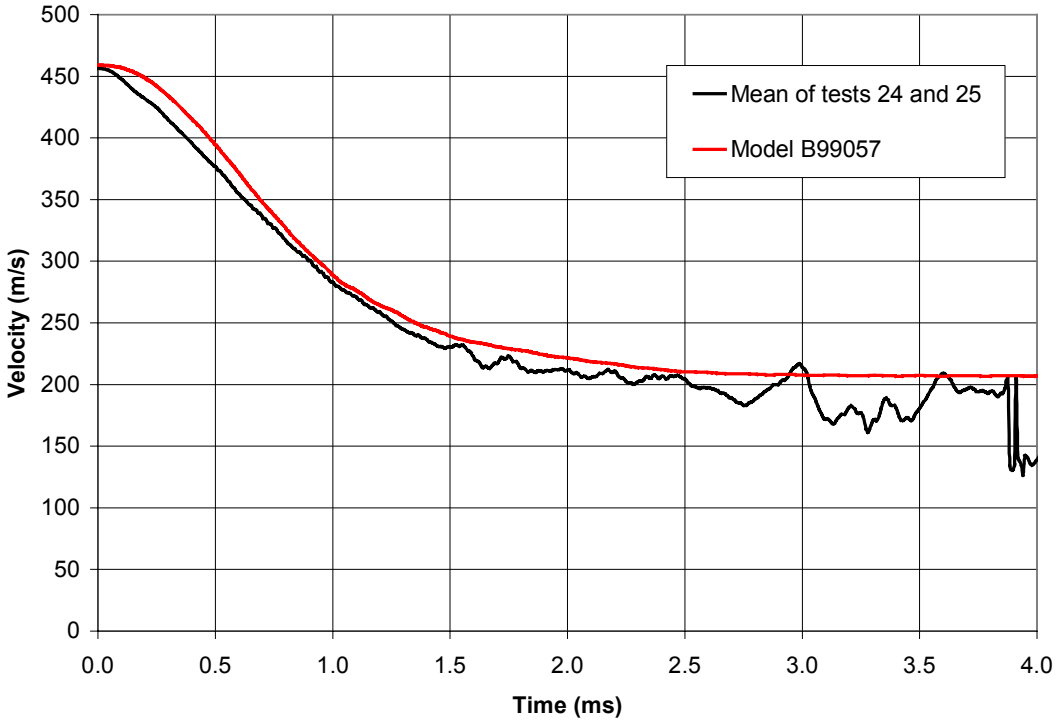

Figure 4.18. Comparison between calculated velocity for model B99057 and data from radar measurement.

Damage plots for models with different damage parameters are shown in figure 4.19. The models show the same behaviour as for the models with 10 mm element size. For the model with EMI's recommended damage parameters there is a quite large damage area with a diameter of approximate 0.80 m. For the model that allows a larger plastic strain before damage occur, there is a decrease of the damaged area to 0.50 m diameter. Compare these damage plots with the photos of the target in figure 4.5.

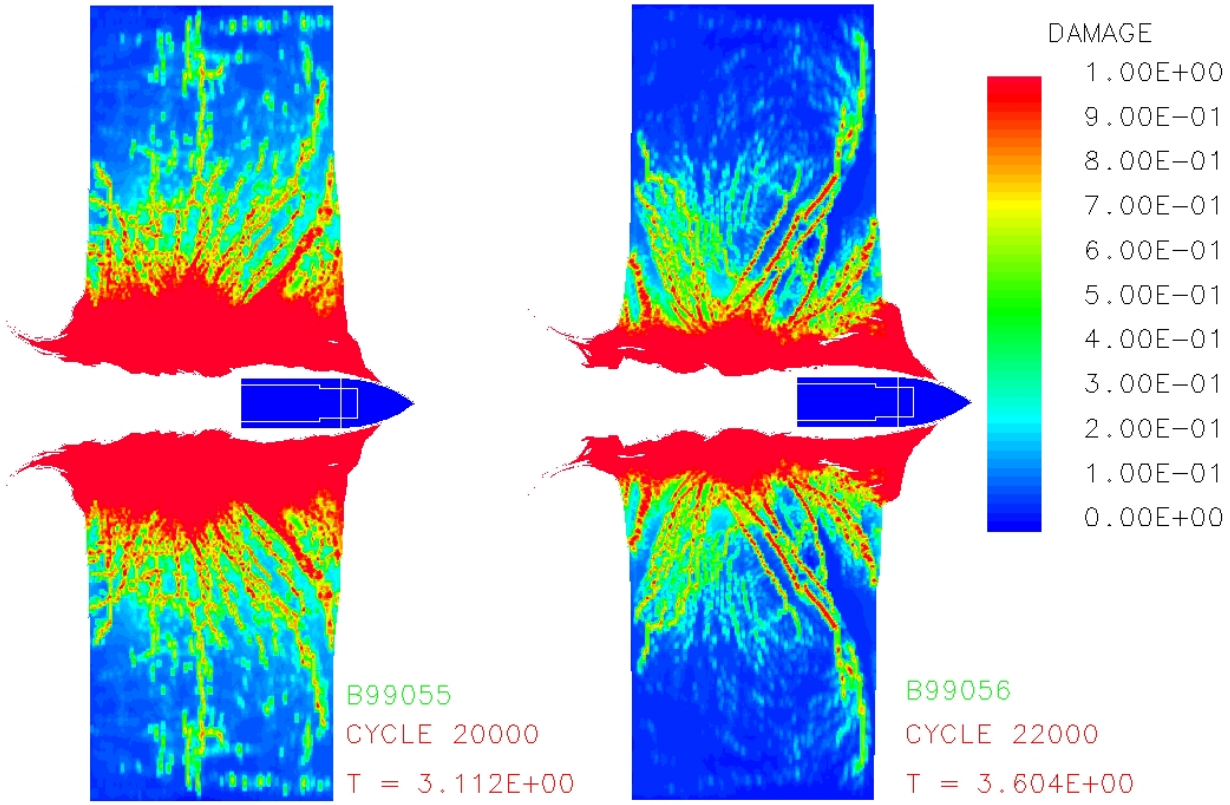

Figure 4.19. Damage plot for models B99055 (left) and B99056 (right) with 5 mm Lagrange elements.

Numerical simulation with Eulerian formulation for the target

The use of an Eulerian target formulation has one major advantage compared with a Lagrangian formulation, and that is the fixed element mesh. Instead of deforming the elements with the material looked inside as for Lagrange formulation, there is a transport of material between fixed elements for the Euler formulation. In this case the projectile is modelled with Lagrange and a contact polygon is defining the interaction surface between projectile and target. The calculation time for models with 5 mm Euler elements is approximate 2.5 h on a Pentium III 800MHz, which is almost 1.5 h shorter than for the model with Lagrange elements of the same size. This is due to the reduced time step for the Lagrange model caused by the deformed elements. One disadvantage with the implementation of Euler formulation in Autodyn is that it is not possible to use friction between the projectile and target. However, due to the large shear forces obtained in Lagrange elements close to the contact surface the use of friction for the Lagrange formulation is limited. The Euler models have generally an increased exit velocity when compared to the Lagrange models with the same material properties. This might be due to the transportation algorithms that allow material to flow between elements. The parameters for the calculated Euler simulations are compiled in tables 4.8 and 4.9.

Table 4.8. Model properties for simulations with Euler elements in target, except when other values are specified. The material properties and projectile subgrid are the same as for the Lagrange models, see table 4.5.

Models	**B99E03-B99E05**	**B99E55**
Element type	Eulerian target formulation Lagrange projectile formulation	
Element size in target	10×10 mm	5×5 mm elements for radius < 500mm *.
No. of elements in target	125×120=15,000	200×160=32,000
Filled elements in target	75×120=9,000	150×160=24,000
Size of target (Euler) subgrid	1.25 m × 1.20 m	
Friction coefficient	No friction	
Erosion strain	No erosion	

Note: * Graded element lengths used in radial direction, 5-22 mm and graded element lengths in axial direction for empty elements, 5-13 mm

Table 4.9. Euler models of benchmark tests.

Model	**B99E03**	**B99E04**	**B99E05**	**B99E55**
Element size	10 mm			5 mm
Residual strength constant B	1.60	1.90	1.60	
Residual strength exponent M	0.61	0.60	0.61	
D_1	0.04		0.08	
EFMIN	0.01		0.05	
Exit velocity	265 m/s	237 m/s	246 m/s	255 m/s
Energy error	0.2 %	0.5 %	0.3 %	0.1 %

The damaged area is approximate 0.6 m in diameter for the model B99E55. Compared with the Lagrange models, the shape of the damaged area is more shaped like a hour glass for the Euler model. Compare the damage plot with the photos of the target in figure 4.5.

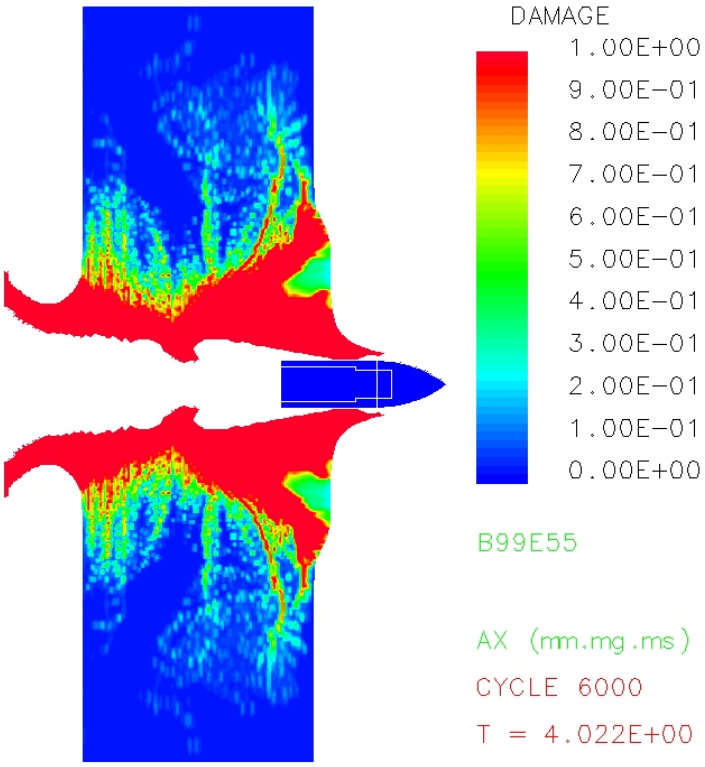

Figure 4.20. Damage plot for model B99E55 with 5 mm Euler elements.

Numerical simulation with SPH formulation for the target

Numerical simulations of the benchmark tests were also performed with SPH formulation, these models were not reported in the earlier technical report. The advantage with SPH compared with Lagrange is that the formulation is mesh less, and thereby the problem with distorted elements is eliminated. The advantage compared with Euler formulation is that the material is located to the same node during the simulation, therefore the same material models and failure conditions as for Lagrange can be used for SPH. However, for materials that can sustain large tensile strains the SPH model can develop a numerical failure due to loss of contact between the nodes in the model. For penetration in concrete and ceramics this problem doesn't occur due to the low failure strains during tensile loading for this type of materials. The material properties and projectile subgrid are the same as for the Lagrange models, see table 4.5. Both models with and without friction were used, see table 4.10. Damage plots for the models are shown in figure 4.21.

Table. 4.10 Models with 5 mm SPH nodes of benchmark tests.

Model	**B99S00**	**B99S01**
Element size in target	5 mm SPH nodes	
Number of nodes in target	150×240 nodes	
EFMIN	0.05	
D2	0.08	
Residual strength constant B	1.60	
Residual strength exponent M	0.61	
Friction coefficient	No friction	0.05
Erosion strain	No erosion	
Gap size	1.1 mm	
Exit velocity	214 m/s	186 m/s
Energy error	0.5 %	9.2 %

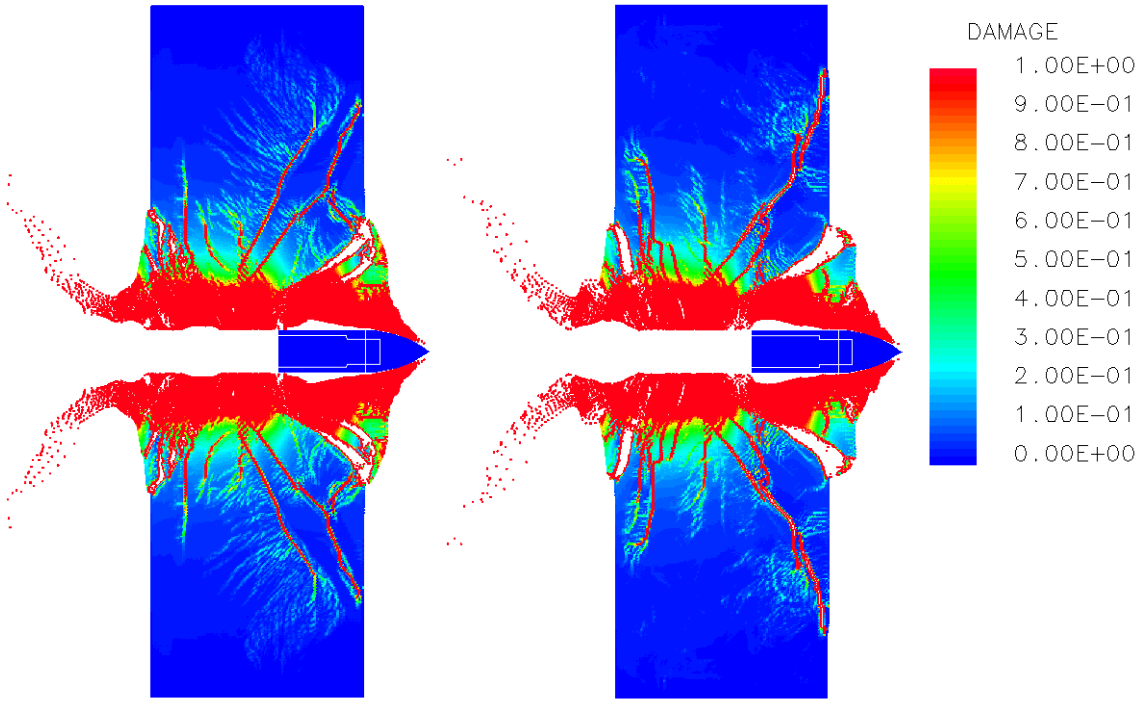

Figure 4.21. Damage plot for models B99S00 without friction (left) and B99S01 with friction (right), both models simulated with 5 mm SPH nodes.

5. MATERIAL MODELLING OF CONCRETE WITH APPLICATION TO STRUCTURAL RESPONSE

Drop weight tests were performed within the project 1999 at FOI (FOA) in order to get a data for verification of tools for numerical simulations. These tests were simulated numerically using the commercial finite element code LS-Dyna together with a mechanical constitutive model for concrete called K&C Concrete model. The purpose of this study was to evaluate the ability of the chosen numerical method and material models to predict the material and structural response. This work is presented here.

5.1. Drop weight tests

In the tests performed at FOI in 1999, four reinforced concrete beams were subjected to impact loading using a drop weight, see figure 5.1. For comparison also quasi-static loading was used for three beams. The test set-up and results are presented in Ågårdh et al (1999) and Magnusson et al (2000). The length of the beams was 4.2 m with simply support 0.1 m from the ends. The cross section of the beams was 0.17x0.34 m. The drop weight had a mass of 718 kg, and the cylindrical striker head impacted a steel pad fixed to the beam at 6.7 m/s. Hydraulic dampers were used to stop the drop-weight after 90 mm of vertical displacement of the beam, corresponding to approximately 20 ms after impact. The reinforcement of the beams consisted of two ø12 mm rebars with the centre 71 mm from top surface of the beam, and two ø12 mm rebars with the centre 31 mm from the bottom of the beam. Shear reinforcement consisting of 11ø10 mm stirrups with a c/c distance of 150 mm was used from 0.10 to 1.60 m from both ends of the beams, leaving 1.0 m of the beam at mid-span without shear reinforcement, see figure 5.2. The following registrations were made during the tests:

Displacement history and crack localisation from high speed photos of the beam mid-section.

Displacement and acceleration history for drop weight striker.

Indication of contact between striker head and impact pad.

Beam acceleration history 100 mm to the left and right of mid-span.

Beam displacement history at mid-section.

Crack indication of concrete.

Strain history in lower reinforcement rebars 200 mm from mid-span and at mid-span.

Strain history at the concrete surface at mid-span at the same height as rebars placement.

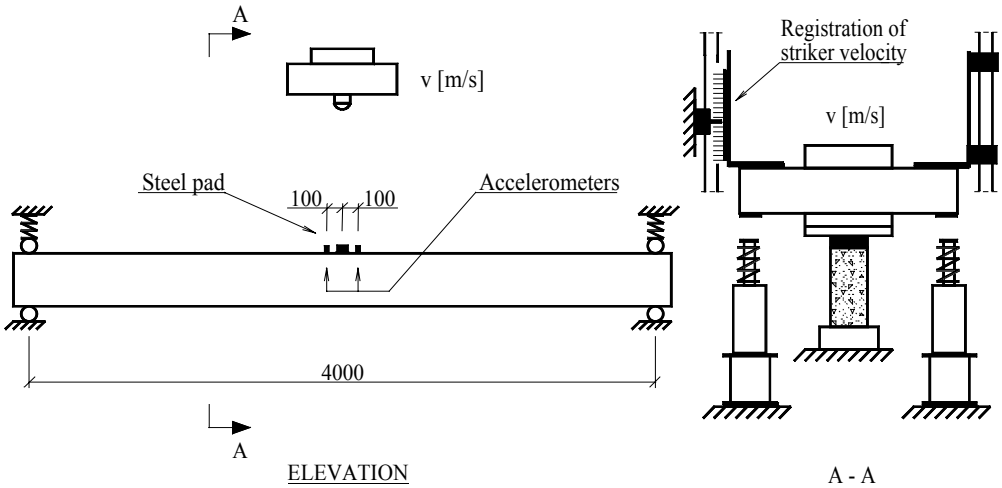

Figure 5.1. Drop weight test set-up with dimensions in mm.

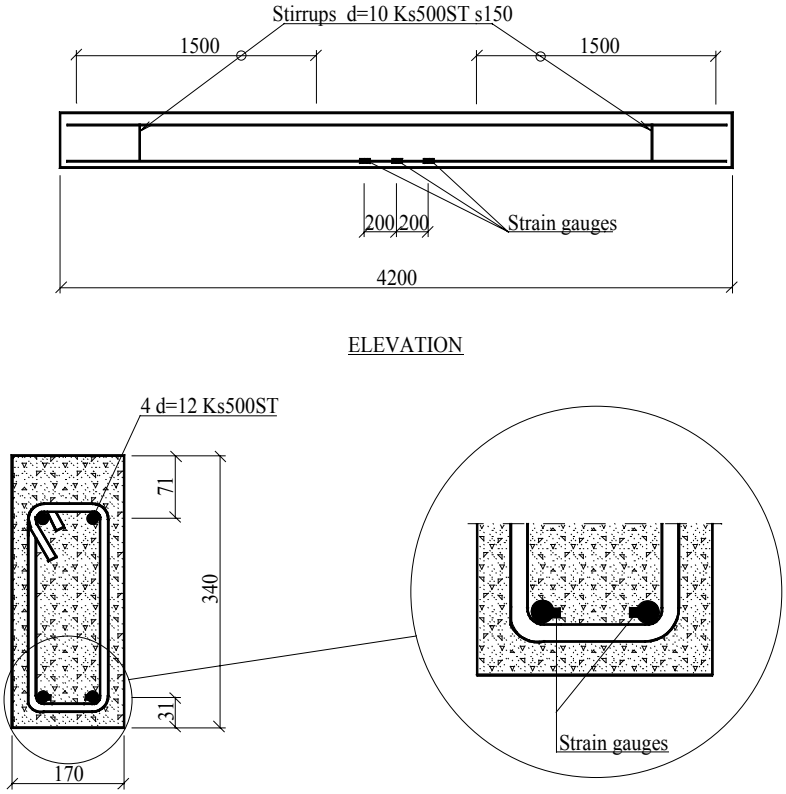

Figure 5.2. Reinforcement locations and cross section for concrete beams with dimensions in mm.

5.2. Material properties and modelling

The concrete material and steel material for the reinforcement were characterised to obtain data for the numerical analysis of the reinforced concrete beam.

5.2.1. Concrete properties and modelling

The used concrete type was the same as the one used for the targets for the benchmark projectile perforation tests described in chapter 4 earlier. The concrete were mechanically characterised at several occasions through weighing of test specimens, uniaxial compression of 150x150 mm cubes and ø100x200 mm cylinders and split tensile tests on 150x150 mm cubes. The fracture energy release was determined from RILEM beam testing (Hilleborg, 1985). Confined uniaxial compression of ø75x150 mm cylinders was performed by the Norwegian Defence Research Establishment (FFI) and Imperial college in London with the gauged reactive confinement (GREAC) cell, see chapter 4.2.1. The Poisson's ratio was taken as 0.16 and the tensile strength taken as 0.8 times the splitting strength. The material properties are summarised in table 5.1.

Table 5.1. Mechanical properties for the concrete.

Density	**Modulus of elasticity**	**Poisson's ratio**	**Compressive strength**	**Tensile strength**	**Fracture energy**
2420 kg/m^3	44 GPa	0.16	100 MPa	5.2 MPa	156 N/m

To model the concrete material the K&C concrete model release III was used (Malvar et al, 1997). The source code for this model was made available to FOI through an agreement with the developers. Release I of the K&C model is available as a standard material model in LS-Dyna. The input parameters for the material model needs to be determined for each used element size, and according to this several material definition have to be used in the numerical model when different element sizes is used. Modifications were made to the material model to scale the plastic deformation relative to the size of the current element during the unstable cracking and softening phase of the material. This resulted in a material model with a energy release during cracking that is independent of the used element size.

In the model, the elastic material properties, except for the Poisson's ratio, are derived from the equation of state. The experimental data of the pressure-density relationship was complemented with two data points to get a correct elastic wave speed and to get a correspondence with the uniaxial data on the modulus of elasticity. The first linear elastic part of the equation of state was constructed using results from uniaxial tension tests. The volumetric strain, pressure and unloading bulk modulus for the first point were calculated as:

$$\varepsilon_v = \frac{0.4 f_{cc}}{E_c}(2\nu - 1) = \frac{0.4 \cdot 100 \times 10^6}{44 \times 10^9}(2 \cdot 0.16 -) = -0.00062$$

$$p = -\frac{0.4 f_{cc}}{3} = \frac{0.4 \cdot 100 \times 16^6}{3} = 13.3\ MPa$$

$$K_u = \frac{E_c}{3(1-2\nu)} = \frac{dp}{d\varepsilon_v} = 21.5\ GPa$$

The second additional point as:

$$\varepsilon_v = -0.0022$$

$$p = -\frac{f_{cc}}{3} = \frac{100 \times 10^6}{3} = 33.3\ MPa$$

$$K_u = \frac{dp}{d\varepsilon_v} = \frac{33.3 \times 10^6}{0.0022} = 15.2\ GPa$$

These points where then connected to the experimental data from the GREAC cell tests and the resulting input equation of state together with loading and unloading bulk modulus are shown in figure 5.3 and table 5.2.

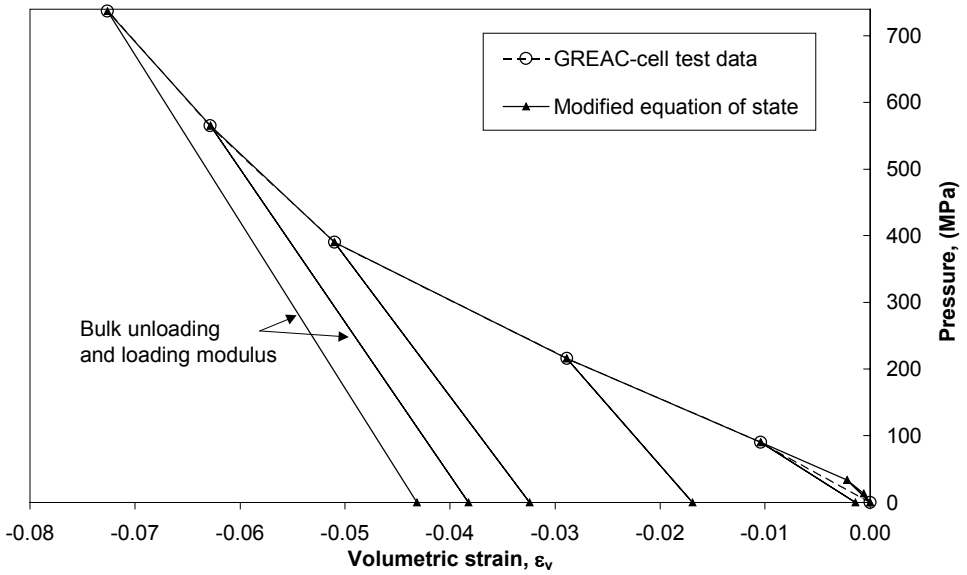

Figure 5.3. Input equation of state with test data from GREAC cell test performed at FFI.

Table 5.2. Tabulated equation of state with loading and unloading bulk modulus.

Mass density (kg/m^3)	**Relative volume** (-)	**Volumetric strain** (-)	**Pressure** (MPa)	**Bulk modulus** (GPa)
2 390	1.0000	0.0000	0	21.57
2 391	0.9994	-0.0006	13.3	21.57
2 397	0.9978	-0.0022	33.3	15.15
2 415	0.9896	-0.0104	90	10
2 460	0.9715	-0.0289	216	18
2 515	0.9503	-0.0510	390	21
2 545	0.9391	-0.0628	565	23
2 570	0.9300	-0.0726	737	25

The strength surfaces were constructed according to the instructions for the material model and tuned so that the stress path from the unconfined uniaxial compression tests was replicated. Also, the residual strength curve was fitted to the GREAC cell test results at high pressures. These strength surfaces are valid only for pressures above one third of the unconfined compressive strength, so the first point on the unconfined compression stress path has no significance. In figure 5.4 the resulting compression meridians are shown.

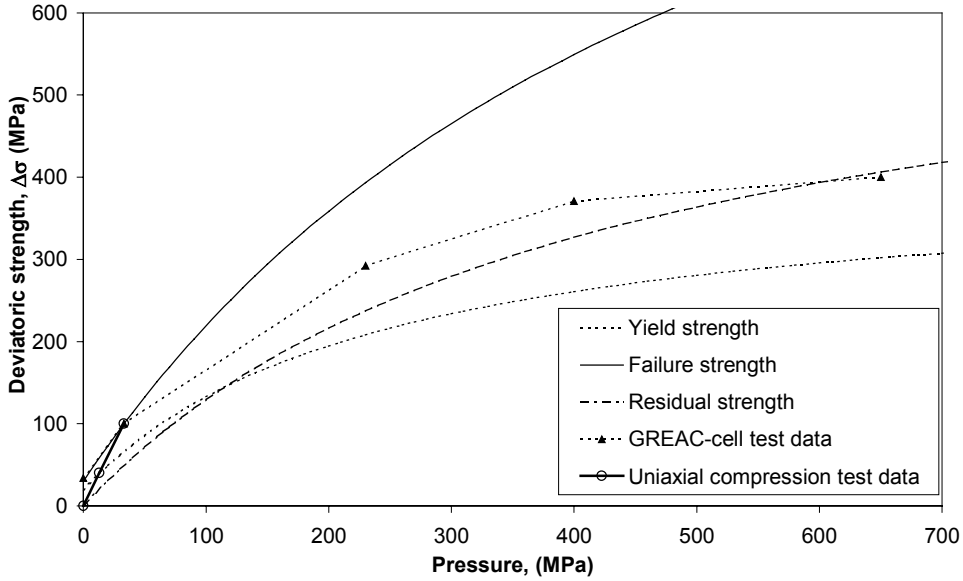

Figure 5.4. Compressive meridians fitted to the unconfined uniaxial and GREAC-cell test data.

To interpolate between these surfaces, i.e. to model the stable and unstable cracking, the model needs the input of a damage function η(λ), see equation 4.1.

$$\Delta\sigma = \eta(\Delta\sigma_{\max} - \Delta\sigma_{\min}) + \Delta\sigma_{\min} \tag{4.1}$$

where $\Delta\sigma = \sqrt{3J_2}$

The modified effective plastic strain λ is calculated according to equation 4.2 below.

$$\lambda = \begin{cases} \displaystyle\int_0^{\bar{\varepsilon}_p} \frac{d\bar{\varepsilon}_p}{r_f\left(1+\frac{p}{r_f}f_{ct}\right)^{b_1}} \; for \; p \geq 0 \\ \displaystyle\int_0^{\bar{\varepsilon}_p} \frac{d\bar{\varepsilon}_p}{r_f\left(1+\frac{p}{r_f}f_{ct}\right)^{b_2}} + b_3 f_d k_d (\varepsilon_v - \varepsilon_v^{yield}) \; for \; p < 0 \end{cases} \tag{4.2}$$

where

$\bar{\varepsilon}_p = \sqrt{\frac{2}{3}\varepsilon_{ij}^p \varepsilon_{ij}^p}$

$p = -\frac{1}{3}tr(T)$, where T is the stress tensor

r_f is the strain enhancement factor

f_{ct} is the strength in uniaxial tension

k_d is the internal scalar multiplier

$$f_d = \begin{cases} 1 - \frac{\left|\sqrt{3J_2/p}\right|}{0.1} & for \left|\sqrt{3J_2/p}\right| < 0.1 \\ 0 \quad for \left|\sqrt{3J_2/p}\right| < 0.1 \end{cases}$$

b_1, b_2 and b_3 is curve fitting parameters.

Simulations of uniaxial extension and compression of a single cube element was performed during which the damage function was altered until the right fracture energy release and the maximal crack opening, according to test data and the recommendations in the CEB-FIP model code 90, were obtained. The resulting damage function is given in figure 5.5 and table 5.3.

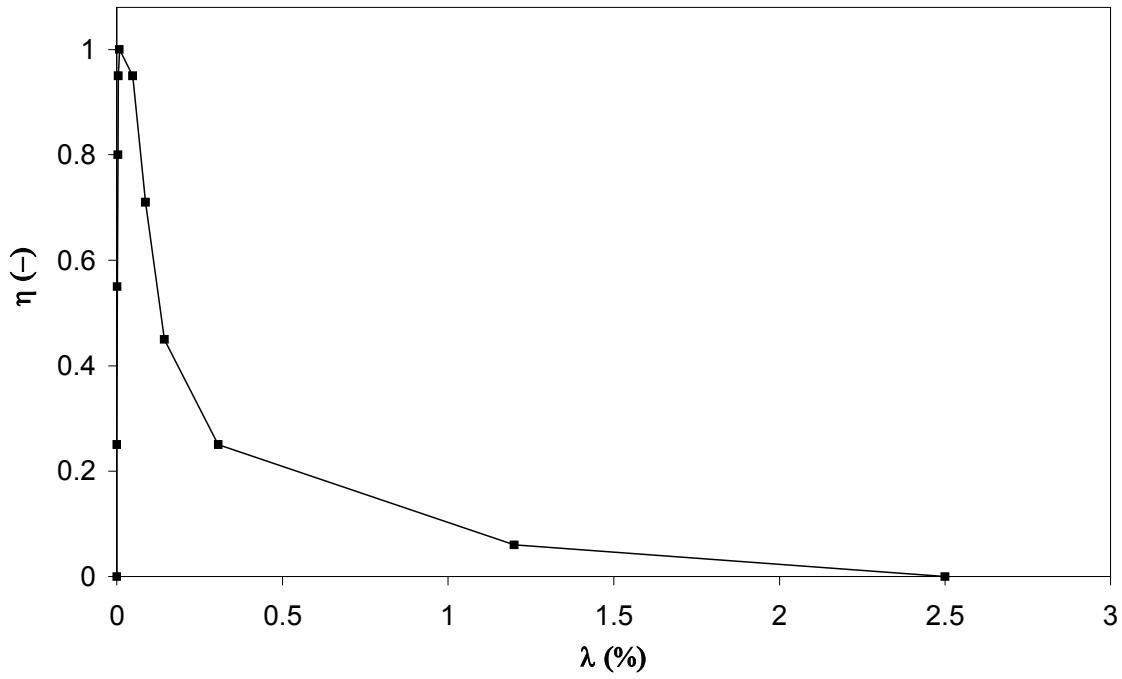

Figure 5.5. Damage function.

Table 5.3. Tabulated damage function.

λ	0.00	5.50×10^{-6}	1.40×10^{-5}	2.90×10^{-5}	5.10×10^{-5}	8.20×10^{-5}
$\eta = f(\lambda)$	0.00	0.25	0.55	0.80	0.95	1.00
λ	4.80×10^{-4}	8.60×10^{-4}	1.44×10^{-3}	3.06×10^{-3}	1.20×10^{-2}	2.50×10^{-2}
$\eta = f(\lambda)$	0.95	0.71	0.45	0.25	0.06	0.00

The material model incorporates the possibility of strength enhancement due to loading rates and for this the bilinear relation given in the CEB-FIP model code 90 was used. Also, it is possible for the user to set the associativity of the flow rule. This is done via a scalar valued parameter with value 0-1, where 0 gives a volume preserving flow rule, i.e. no dilatancy, and 1 implies an associated flow rule.

5.2.2. Reinforcement properties

The steel reinforcement was characterised through uni-axial tension test of a ø12 mm Ks 500 ST rebar. The density and Poisson's ration were set as defaults according to standard tables. The tests were performed at the Swedish National Testing and Research Institute (SP) according to SS-EN 10 002-1 and the material properties based on the tests are presented in table 5.4.
For the stirrups, a linear elastic-plastic material model with isotropic hardening was used. A linear elastic-perfectly plastic material model with the same elastic properties as above was chosen due to restrictions in the code for the tensile and compressive reinforcement steels.

Table 5.4. Used mechanical properties of the reinforcement steel.

Mass density	Modulus of elasticity	Poisson's ratio	Yield limit	Hardening modulus	Tensile strength
7 800 kg/m^3	207 GPa	0.30	586 MPa	1.0 GPa *	684 MPa *

Note: * Strain hardening is only used for stirrups, no strain hardening for tensile and compressive reinforcement.

5.2.3. Drop weight properties

The drop weight was modelled with a linear elastic material model with a modulus of elasticity of 200 GPa and Poisson's ratio set to 0.3.

5.3. Numerical simulation

The problem was numerically analysed in the finite element code LS-Dyna version 950d. Material, or Lagrangian, description of the motion for the whole problem was used. One-point Gauss integration and viscous hourglass control was also used for the beam and drop weight. For the steel-pad and striker-head selectively reduced integration was used. The reinforcement bars were modelled with beam elements and the stirrups with truss elements. The element size for the beam was gradually increased from 10x10x10 mm in the impact zone to 10x10x100 mm at the beam end. For the problem both double and single symmetries were used.

A surface-to-surface constraint algorithm with friction was used for the two contact interfaces, striker to steel pad and steel pad to beam. For the coupling between concrete and reinforcement the adjacent beam and reinforcement nodes were merged. The hydraulic dampers were not incorporated in the model and the problem was only analysed up to 20 ms after impact. Acceleration due to gravity was used for the problem.

5.4. Results from simulations and comparison with test data

The results from the simulations displayed a different behaviour than the test results. In the test cracks in mode I (tension) were initiated, the first approximately 0.3 ms after impact, at the bottom of the beam followed by crushing of the material in the impact zone. The simulations reproduced the first mode I crack but also displayed an almost instantaneous initiation of a mode II (in plane shear) crack 50 mm from the centre point of impact. This crack then propagated through the beam resulting in a partial separation of the material directly under the striker and the rest of the beam. The shear failure prevents additional mode I cracks to develop and crushing of the impact zone. See figure 5.6 for the damage (cracking) of the beam. A linear equation of state was used to eliminate the influence of porous compaction in the numerical model. However, this did not change the failure mode of the beam.

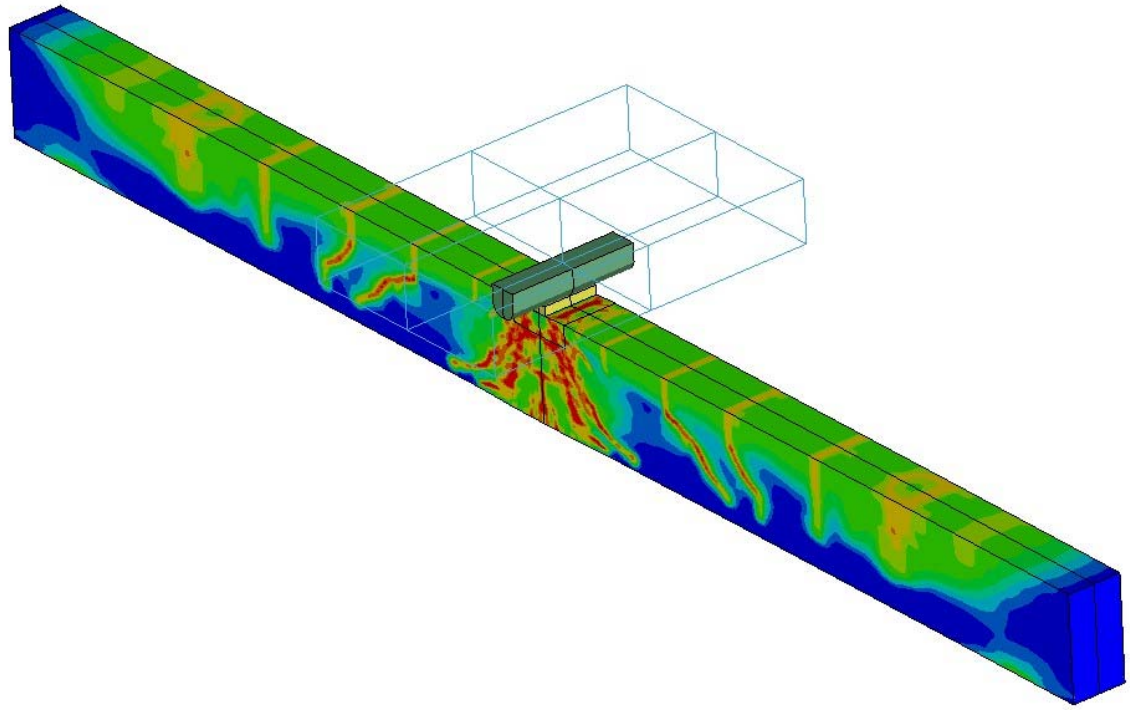

Figure 5.6. Damage localisation for numerical simulation of drop weight impact on beam.

Comparisons are made between the registrations from the test and the corresponding data from the numerical analysis. Comparisons between the high-speed photos and damage plots from the model are given in figures 5.7 and 5.8.

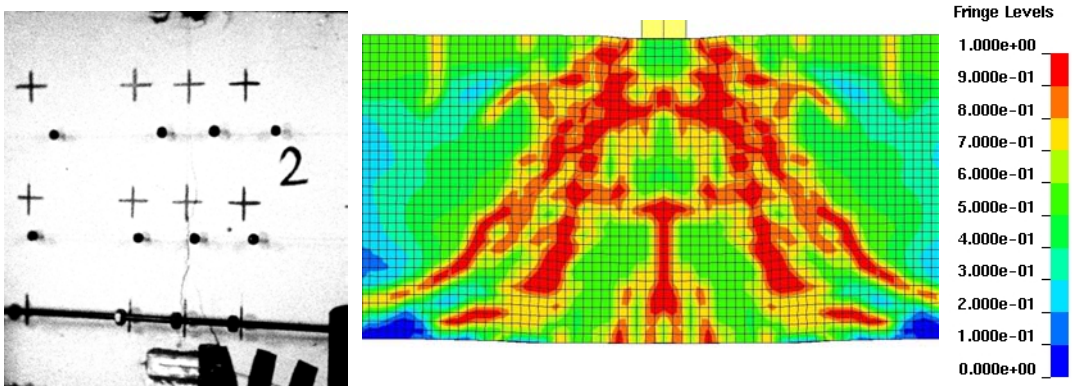

Figure 5.7. High-speed photo at mid-span and numerical damage plot after 0.6 ms.

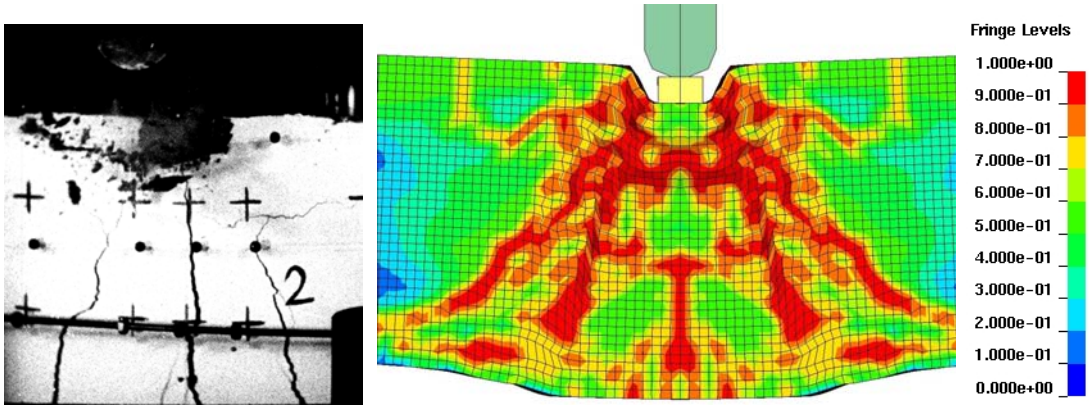

Figure 5.8. High-speed photo at mid-span and numerical damage plot after 20 ms.

In the numerical analysis, the striker displacement is greater the peak deceleration is lower than measured during the tests. This is likely to be due to the shear failure of the beam. A comparison between the measured and calculated striker displacement are shown in figure 5.9.

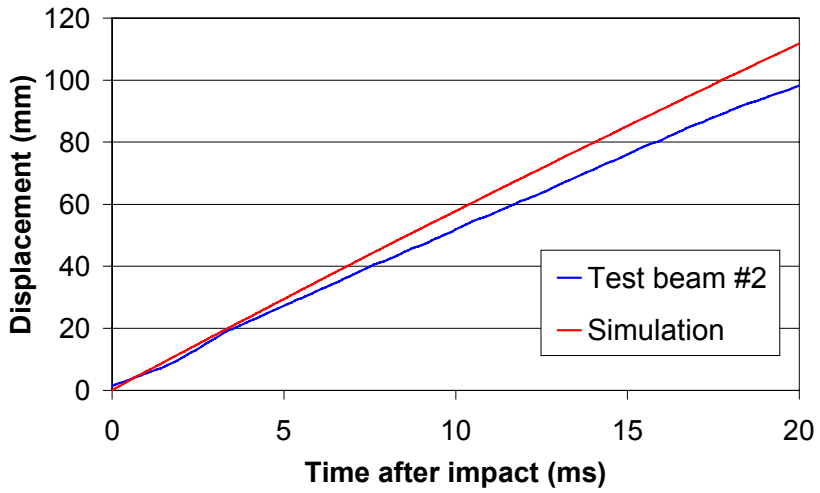

Figure 5.9. Striker displacement from test and simulation.

The data on the nodal acceleration from the simulation was difficult to use for comparisons due to numerical oscillations. In figure the acceleration from the simulation was filtered using averaging over nine points. However, integration of the signals shows that the speed of the beam is lower in the model than in test. Again, this is likely to be caused by the local shearing failure of the beam at the point of impact. This also causes large deformations and displacements at the midsection of the beam. Comparisons between measured and calculated data are shown in figure 5.10.

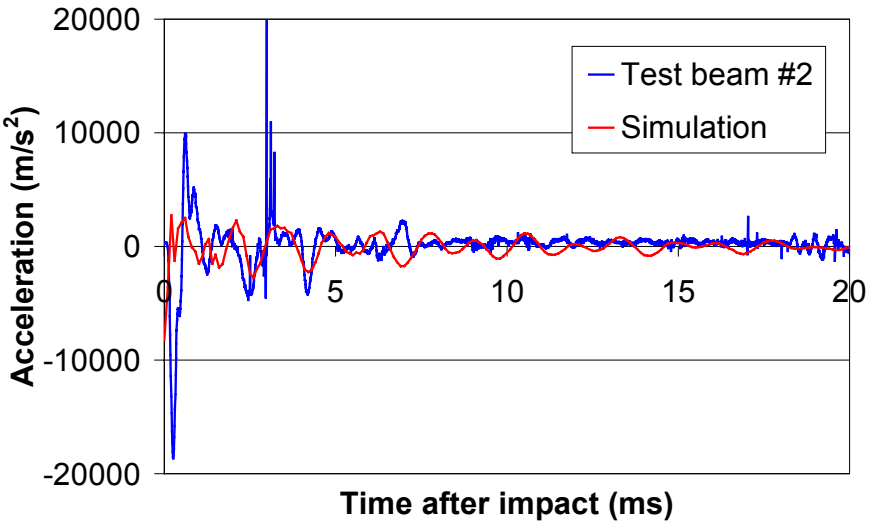

a)

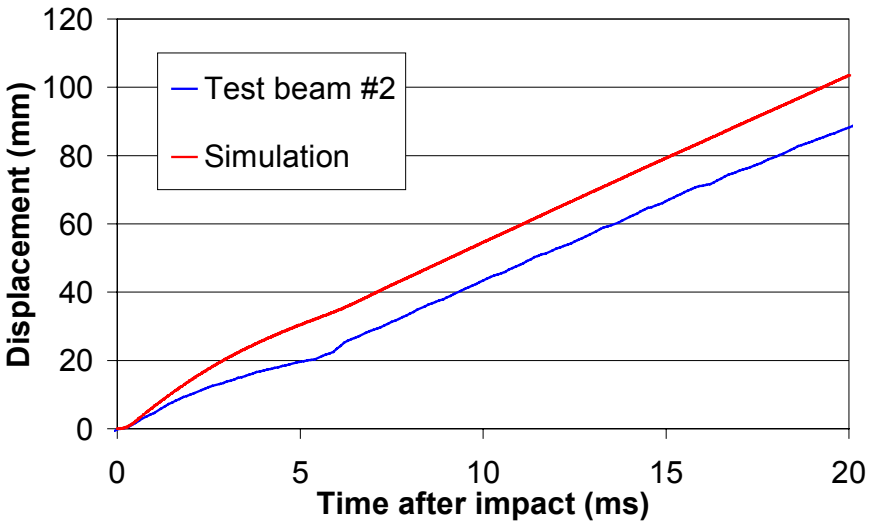

b)

Figure 5.10. Beam acceleration histories from test and simulation (a), and beam mid-section velocity histories from test and simulation (b).

For the mode I crack at the beam's lower surface, the model reproduces well the time for the initiation. The stress-strain relationship shown in figure 5.11 reveals that the material behaviour in tension is accurately described in the model.

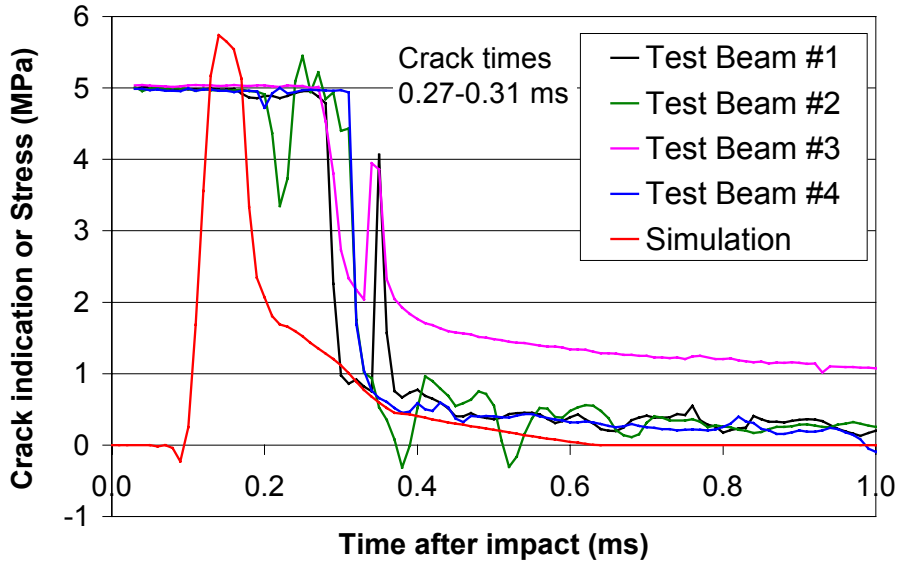

Figure 5.11. Crack indication from test and stress history from simulation at beam mid section.

The initial strain in the concrete for the model is slightly smaller than measured for the tests, with the gauge reaching its maximum range after approximate 0.5 ms. A comparison between the measured and calculated strains in the concrete at the same height as the tensile reinforcement are shown in figure 5.12.

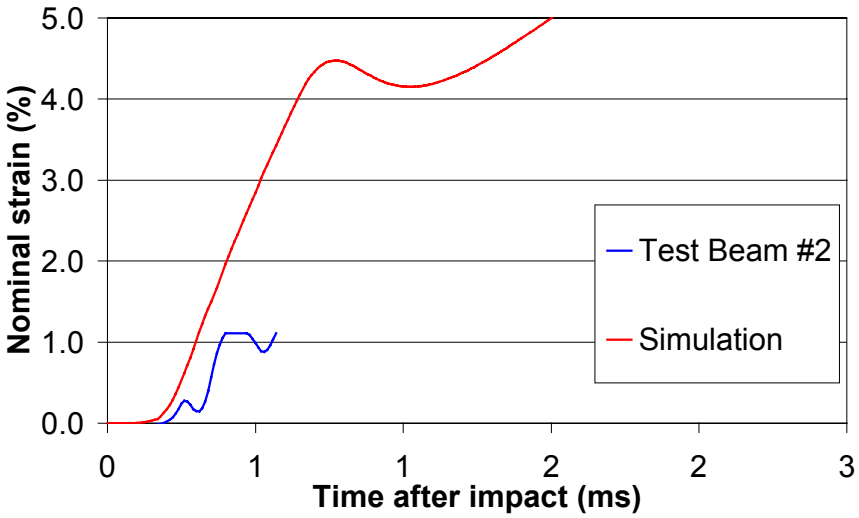

Figure 5.12. Strain histories in concrete at beam mid section at the same height as the tensile reinforcement.

The calculated strain in the lower reinforcement steels 200 mm from mid-section show an acceptable agreement with the test in the initial phase. The strain histories calculated for the reinforcement at the midsection show a good agreement with the test results initially. However, the strain gauges reaches their maximum ranges approximate 1 ms after impact. The measured and calculated strains for the steels are shown in figure 5.13.

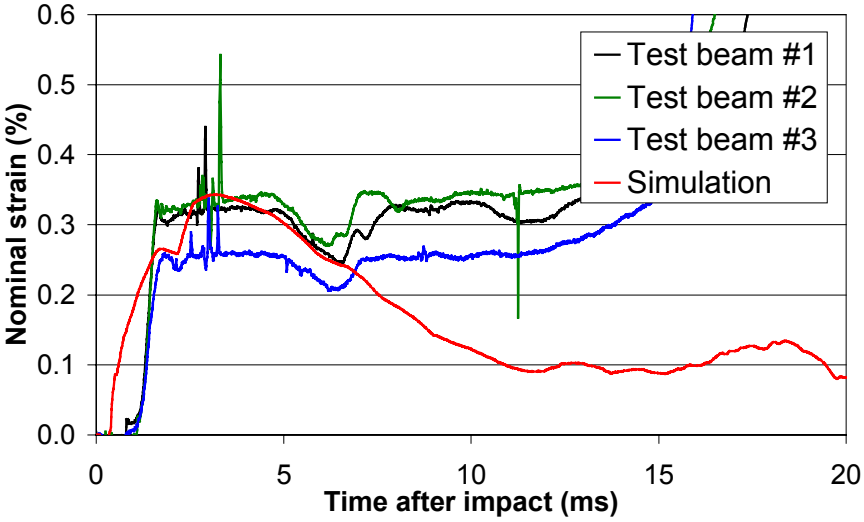

a)

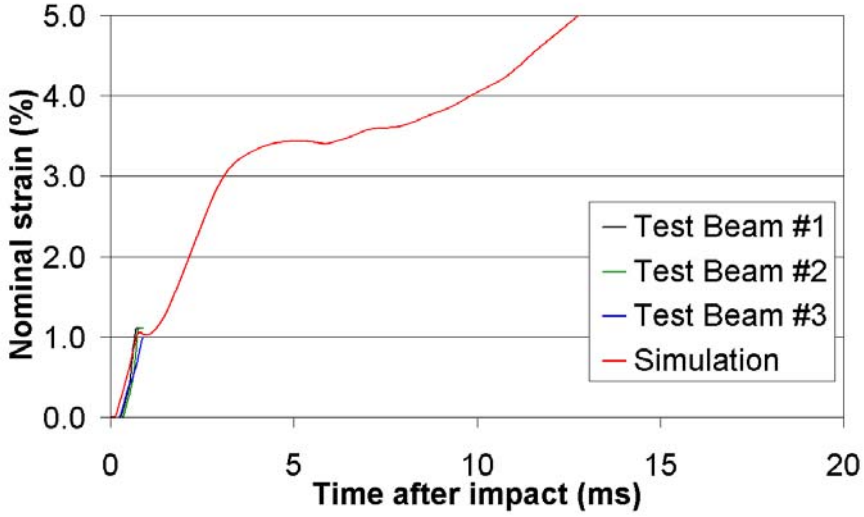

b)

Figure 5.13. Strain histories in lower reinforcement steels 200 mm from beam mid section (a), and at beam mid section (b).

6. MATERIAL TESTING AT HIGH PRESSURES AND DEFORMATION RATES

Material testing were performed at EMI for the HPC developed at FBT in Norway. The dynamic properties of the aggregate and mortar for the HPC were determined, and with the use of mesomechanical modelling the material properties of the HPC were calculated. This type of material testing followed by numerical simulation to determine the properties of a mixture, i.e. concrete, seems very useful for determination of material properties for complex materials.

The properties of aggregate and mortar are determined with inverse plate impact tests and quasi-static tests with confined mortar. Inverse plate impact tests are performed by shooting a sample of the test material against a witness plate of known material i.e. aluminium, see figure 6.1a. In figure 6.1b a projectile with a mortar sample is shown. The maximum impact or particle velocity that was used for the plate impact test was 1050 m/s, this created stresses in the sample up to 6.9 GPa. Greater deformation velocities can be obtained with the use of explosive loaded test samples. However, stresses above 5 GPa does normally not occur during penetration in concrete by rigid projectiles. Riedel (2000, 1999) has shown a good agreement between the calculated macroscopic dynamic behaviour of concrete and earlier published data from the literature. A comparison with data from static and inverse plate impact is shown in figure 6.2. The test of the concrete developed at FBT gives an opportunity to obtain high quality dynamic material properties for numerical modelling of penetration phenomena.

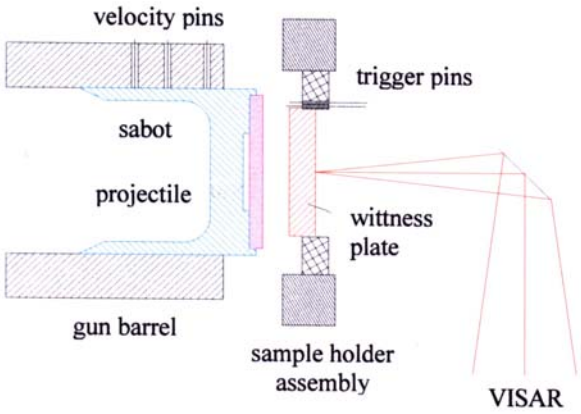

a) b)

Figure 6.1. Setup for inverse plate impact tests (a) from Thoma et al (1999), and projectile with mortar sample (b).

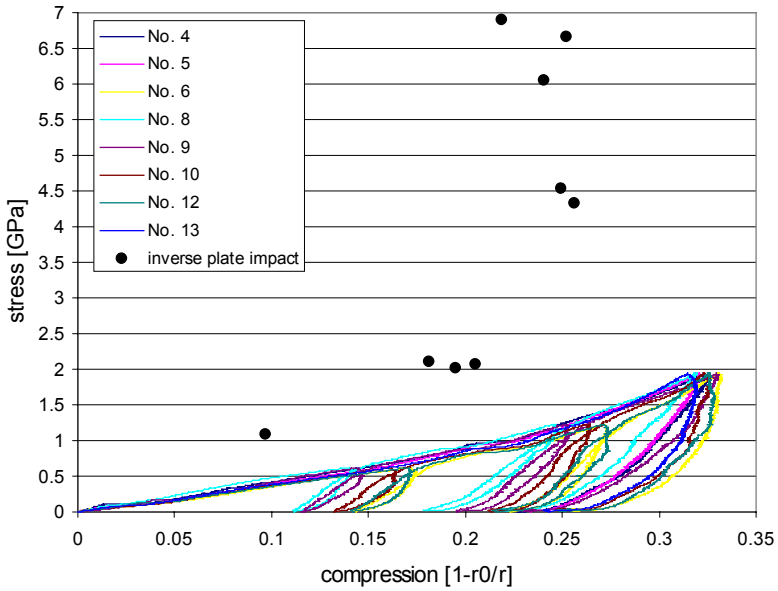

Figure 6.2. Comparison between data from quasi-static and inverse plate test of mortar for HPC.

7. SUMMARY AND FUTURE RESEARCH

The development of parallel computers based on clusters has increased the possibility to obtain computer capacity for advanced simulations at a reasonable expense. These parallel computations are performed with standard personal computers running Windows 2000 or Linux operating system, and connected through a local area network. This reduces the computational cost considerable in comparison with high level Unix workstations, and gives the opportunity to use three-dimensional advanced models for computer simulations at a reasonable cost.

The Lagrange element formulation is not suitable for large deformation since the element mesh moves with the material and therefore gets heavily distorted during the simulation. Therefore, it is necessary to use numerical erosion to delete distorted elements, otherwise it is not possible to obtain a solution. With the latest development in material and numerical modelling it is possible to use alternative element formulation in combination with advanced material models. Autodyn can i.e. use the RHT concrete model combined with Lagrange, ALE, Euler and SPH formulation.

The advantage with SPH formulation is that although it in principle is Lagrangian, it is not necessary to use numerical erosion. Preliminary results are very promising, especially when eroding fragments or projectiles are simulated. This formulation makes it possible to retain the mass of both target and an eroding projectile during the simulation, if both parts are modelled with SPH.

7.1. Penetration of steel

The results from the study show that the numerical and physical input data can be used to calculate the ballistic properties for other combinations of rigid projectiles against varying HNS plate thickness. However, the used numerical models with Lagrange formulation can not be used for other steels or other projectiles without experimental verification.

The calculated ballistic limit for the 5.56 mm AP ammunition against a 10.8 mm thick HNS armour plate using user subroutine (Westerling, 2001) is close to 750 m/s for the 0.2 mm element size, while the experimentally result is 762 m/s. The calculated ballistic limit with the use of the Autodyn 2D version 4.2.02 with corrected strain rate behaviour is close to the one obtained for the user routine implemented at FOI. For a 0.1 mm element size in both projectile and target the ballistic limit is decreased with 15-20 m/s.

7.1.1. Material description and models

The nitrogen alloyed steel used in this work was tested in “as received” conditions and is shown to have protective capacities comparable to a conventional RHA of similar hardness. However, cold worked and annealed nitrogen alloyed steels have been reported to have a very high yield strength of 3380 MPa as discussed by Lach et al (1997) with remaining ductility. This indicates a potential for the material for future protective structures and armours. Investigating the ballistic properties of such steel would be an interesting future work. This must be done in close connection between experimental and computational work.

The modified user implementation of the Johnson and Cook strength model in Autodyn 2D version 4.1.13c reproduces the strain rate enhancement more appropriate than the original implementation. The comparison between the numerical results of the stress-strain curves for a simple tensile test at different strain rates with the analytical solution shows that the match is almost exact using the new improved implementation. The original implementation however, gives almost the same stress-strain curves regardless of strain rate. It is also found that the two methods give significantly different results for a more complex case, with a rigid projectile penetrating a steel plate.

7.1.2. Numerical simulation of steel penetration

It is emphasised that the Johnson and Cook model parameters are extracted at strains and strain rates that usually are small compared to the ones found in penetration cases. The experimental data used to extract the parameters for the high nitrogen alloyed steel is here limited to strain rates up to 800 s^{-1} and strains up to about 25 %. If the geometry change during the necking process is known it is possible to determine the stress-strain relations at significantly higher strains and strain rates. As discussed, the numerical models uses extrapolations to very high strains and the maximum strain rates are in the vicinity of 10^5 s^{-1}. Although the penetration results shown here indicate that in some cases the Johnson and Cook model can be used for extrapolations to high strains and strain rates. However, some verifying experimental ballistic work must also be conducted.

It is noted that numerical problems associated with the Lagrange formulation of the penetration problem can affect the result. The standard method to avoid this is to use a erosion criteria, which simply removes the cell at a specified amount of deformation. The numerical erosion criteria can act as an extra failure condition and thus affect the solution of the problem. In this work, a tensile strain criteria of 120 % was used as a failure model for the HNS material and it is emphasised that the numerical choice of erosion strain (150 %) may give a non negligible effect on the penetration calculations. However, using these values the calculated ballistic limit agrees reasonable well with the experimentally found value.

Using an Eulerian formulation of the problem where the material is allowed to flow through the mesh, which remains intact thus avoiding net distortions, is likely to be an improvement. Future penetration simulations should therefore be based on an Eulerian approach where the material is allowed to pass through the elements, thus avoiding element distortions. A more accurate failure model is necessary and must be able to describe damage evolution and fracture. In this area, work has been done by Johnson and Cook (1985) and this model should be adequate for ductile steels such as nitrogen alloyed steels. Material parameters for this failure model is published for several metals, and experimental methods are developed to determine the parameters for other steels, i.e. HNS. Implementation of this model in Autodyn should increase the accuracy of future simulations of penetration in metal armours.

To verify the behaviour of the numerical models it is necessary to compare these with perforation experiments performed on material with known properties, i.e. 4340 steel. This gives an opportunity to identify errors in the numerical simulations.

7.2. Penetration of brittle material, i.e. concrete

7.2.1. Material description

The RHT concrete material model in Autodyn 4.2.00v performs well for simulation of standard tests, i.e. uni-axial compressive stress, uni-axial strain and hydrostatic pressure. However, there seems to be further room for improvements for the tensile behaviour and failure. For now it seems to be the best general available material model for simulation of concrete behaviour during penetration. The material model should be tested further after the general release of Autodyn 2D version 4.2 with the RHT model. A quick check of the general release version was performed with a rerun of model B99057, this resulted in an almost identical exit velocity for the model.

The material properties for high deformation rates and pressures are difficult to determine, and because of this it is difficult to estimate the values for parameters to material models. In this area it is necessary with further research to determine the properties of concrete for large strains, high strain rates and pressures associated with projectile penetration. The equation of state should be determined with dynamic testing, i.e. with plate impact tests and mesomechanical modelling as described earlier. For the simulations performed of the benchmark tests the pressure-density relationship was determined by quasi-static loading.

The pure shear strength should be determined for the concrete, because of this parameter is useful when the pressure dependent yield surface is determined. The shear strength of the used concrete for the benchmark test was not available for the simulations.

One of the parameters that influences the calculation result greatly is the residual strength of the failed concrete. Because of this it is necessary to develop testing methods to determine damage development in the concrete and strength of damaged or partly damaged concrete.

7.2.2. Numerical simulation of penetration in concrete

For the simulations performed with the Lagrange element formulation it is necessary to use numerical erosion to obtain a solution by deleting distorted elements. Because of this, the mass and confinement in the model decreases during the calculation. This has a large influence on the simulation results, at least when advanced material models with pressure dependent yield and/or failure is used. Therefore, numerical erosion should be avoided. The distorted elements in the model also reduce the time step in the simulation, and thereby increase the time for the calculation. This can be done with the use of Eulerian or SPH (Smooth Particle Hydrodynamics) formulation.

Simulations with Eulerian and SPH formulation for the concrete targets, and the use of the RHT concrete model have shown promising results. With these methods it is possible to start to identify problems regarding the material descriptions. For the simulations performed with Lagrangian element formulation it is very difficult to distinguish between errors caused by numerical problems, i.e. from distorted elements and erosion, and errors caused by the material models. The experiences from this work are also possible to use in other areas regarding penetration, i.e. armour penetration. However, there is need for further research to predict the penetration depths and exit velocities for concrete penetration.

Predictions of weapons effects from tandem warheads and multiple impacts require also more adequate models to be able to predict the target properties after the first charge detonation or projectile impact.

The Euler element formulation was used for the concrete targets with RHT pressure dependent yield concrete model. In this case the target are modelled with an Euler formulation and the projectile with a Lagrange or ALE formulation. For the moment it is not possible to consider friction along this contact surface between the Eulerian and Lagrangian subgrids. The reason for this is that only pressure variable is transferred over the contact surface and no other variables are considered. Further, the nodes on the contact surface can not be deleted during the calculation. Therefore, this set up can only be used with moderate deformed projectiles. There could be a great improvement if friction and erosion for the contact surfaces are included in Autodyn 2D. For numerical simulation of shaped charges it seems that the Euler element formulation may be the best suited.

The simulation of perforation experiments is difficult to perform, especially for experiments with relatively low exit velocities. The reason for this is that the behaviour of the target material and the interaction between target and projectile during the spalling and break through phase are complicated. It is likely that simulations of projectile penetration without perforation will give a more accurate result. However, to be able to do this it is necessary to perform benchmark test without perforation to verify the numerical models against.

7.3. Structural response

An investigation has been carried out to determine if a numerical model with the use of LS-Dyna and the K&C concrete model could be used to reproduce the results from a drop-weight test on reinforced concrete beams. Mechanical material characterisations were performed on both the concrete and the steel reinforcement material, and the parameters for the material model were then adapted to the concrete material model. Simulations were performed to investigate how symmetry, flow rule associativity and the equation of state influenced the results.

The conclusion from this study is that the K&C concrete material model is able to describe material response for standard tests as uniaxial tensile and compressive strengths. However, it is not able to reproduce the structural response in the tests performed with the available data for the material properties. Suggestions for future implementation of the material model are to include:

- The possibility to use full or selectively reduced integration for hexahedral elements. The material model can only be used together with one point hexahedral elements for the current implementation, and this is probably inadequate for the zone near the impact for the used element size.
- Inelastic deformations due to isotropic compression should be included in the models damage evolution, i.e. the volumetric strain from the equation of state.
- Introduce a non-local material deformation for the material model is one way to avoid strain localisation, as in the present problem. A simple method is to calculate local strains and to choose a domain of influence. A weight function is then applied to the local strains in this domain and the resulting, weighted strain is used to calculate inelastic strain. In the present model inelastic strain is represented by a scalar valued damage parameter.

One way to circumvent problems of localisation is to introduce a non-local strain measure. This way the material failure in a finite element depends on the state of a neighbourhood of the element, see figure. In the LS-Dyna version 960 this has been implemented for solid elements with one-point integration. The strain measure is weighted and integrated over the element neighbourhood to obtain the non-local modified effective plastic strain.

REFERENCES

AUTODYN Theory Manual Revision 4. Century Dynamics Ltd. Horsham 2001.

Dieter, G. E., Mechanical metallurgy, 3 ed., McGraw-Hill Inc., ISBN: 0-07-100406-8, 1988.

CEB-FIP model code 1990, Comité euro-international du béton (CEB) et Fédération internationale de la précontrainte (FIP). 1993, Thomas Telford: London.

Hansson, H. and Ågårdh, L., Experimental and numerical studies of projectile perforation in concrete targets. Proceedings Structural failure and plasticity symposium (IMPLAST 2000), Elsevier, Oxford UK, 2000. pp 115-120.

Hansson, H., Numerical simulation of air blast, Proceedings of the 10th International symposium on interaction of the effects of munitions with structures, May 2001.

Hansson, H., Numerical simulation of concrete penetration with Euler and Lagrange formulations, FOI-R--0190--SE, Tumba, September 2001.

Hansson, H. and Skoglund, P., Modelling of steel behaviour with application to armour penetration, FOI-R--0201--SE, FOI, Tumba 2001.

Herrmann, W., Constitutive Equation for the Dynamic Compaction of Ductile Porous Materials. Journal of App Physics, Vol 40, No 6, 1969. pp. 2490-2499.

Hilleborg, A., Determination of the fracture energy of mortar and concrete by means of three-point bend tests on notched beams, Materials and structures, 1985. 13: p. 285-290.

Johnson, G. R., Cook, W. H., A constitutive model and data for metals subjected to large strains, high strain rates, and high temperatures. Proceedings 7th. International Symposium on Ballistics. Holland, 1983. pp. 541-547.

Johnson, G. R. and Cook, W. H., Fracture Characteristics of Three Metals Subjected to Various Strains, Strain Rates, Temperatures and Pressures, Eng. Fracture Mechanics, 21, 1985.

Lach, E., Uggowitzer, P. and Rondot, F., Hardening of Nitrogen Alloyed Steels by Shock Waves, J. Phys. IV France 7, 1997.

Lach, E., Koerber, G., Scharf, M. and Bohmann, A., Comparison of Nitrogen Alloyed Austenitic Steels and High Strength Armor Steels Impacted at High Velocity, Int. J. of Impact Engineering 23, 1999.

Lichtenberger, A. Lach, E. and Rondot, F., Dynamical Behavior of Very High Strength Nitrogen Alloyed Steels, J. Phys. IV France, 1997.

Magnusson, J. and Hallgren, M., High strength concrete beams subjected to shock waves from air blast - Experimental results, Proceedings of the 10th International symposium on interaction of the effects of munitions with structures, May 2001.

Magnusson, J., Hansson, H. and Ågårdh, L., High strength concrete beams subjected to impact load - Some experimental results, Preceding IMPLAST 2000, October 2000.

Malvar, L.J., et al., A plasticity concrete material model for dyna3d. International Journal of Impact Engineering, 1997. 19(9-10): p. 847-873.

Riedel, W.: Ein makroskopishe, modulares Betonmodell für Hydrocodes mit Verfestigung, Schädigung, Entfestigung Drei-Invarientenabhängigkeit und Kappe. EMI-Bericht 7/98. EMI Freiburg 1998.

Thoma, K., Riedel, W. and Hiermaier, S.: Mesomechanical modeling of concrete shock response exreriments and linking to macromechanics by numerical analysis, ECCM conference München, 1999.

Riedel, W., Thoma, K., Hiermaier, S., Schmolinske E., Penetration of Reinforced Concrete by BETA-B-500. Numerical Analysis using a New Macroscopic Concrete Model for Hydrocodes. Proceedings of 9th International Symposium on Interaction of the Effects of Munitions with Structures. Berlin, 1999. pp 315 - 322.

Riedel, W., Beton unter dynamishen lasten, Meso- und makromechanische modelle und ihre parameter. EMI-Bericht 6/00, EMI Freiburg July 2000.

Savage, S. J., Skoglund, P., Eriksson, J. Olsson, L.-G. and Persson, P., Ballistic and High Strain Rate Properties of High Nitrogen Steel Compared to RHA, Proc. 18th Int. Symp. on Ballistics, San Antonio, TX, USA, 1999.

Schmidt-Hurtienne, B. and Eibl, J., A new dynamic damage constitutive law for concrete – Application to split Hopkinson bar tests data and concrete plate perforation experiments. Workshop proceedings from Material test procedures in support of dynamic material modelling. FOA-R--99-01227-311--SE. FOA, Tumba, November 1999.

Skoglund, P. and Savage, S., Constitutive Modeling and Mechanical Properties of a Nitrogen Alloyed Steel, J. Phys. IV France, 10, 2000.

Svensson, T., A Pendulum Impactor for Confident Tensile Testing at High Rates of Strain, FOA C 20577-D4, 1985. (In Swedish)

Svinsås, E., O'Carroll, C., Wentzel, C. M. and Carlberg, A.: Benchmark trial designed to provide validation data for modelling. Proceedings of 10th International Symposium on Interaction of the Effects of Munitions with Structures. San Diego, May 2001.

Willam, K. J., Warnke, E. P., Constitutive Model for the Triaxial Behaviour of Concrete. Seminar on Concrete Structure Subjected to Triaxial Stresses. IABSE Proc. 19, Italy, 1975.

Unosson, M., Numerical simulation of the response of reinforced concrete beams subjected toheavy drop tests, 4th Int. Sym on Impact Engineering, July 2001.

Unosson, M., Modelling of concrete material behaviour with application to reinforced concrete beams subjected to impact, FOI-R--0167--SE, FOI Tumba, October 2001.

Westerling, L., An implicit method for a strain rate dependent constitutive model implemented in Autodyn as a user subroutine, FOI-R--0310--SE, FOI Tumba, 2001.

Ågårdh, L. and Hansson, H., Perforation of steel fibre reinforced concrete slabs with fragments in the velocity range of 1400 – 1600 m/s. Workshop proceedings from Material test procedures in support of dynamic material modelling. FOA-R--99-01227-311--SE. FOA, Tumba, November 1999.

Ågårdh, L. and Hansson, H., Perforation of steel fibre reinforced concrete slabs with steel fragments in the velocity range of 1400 – 1600 m/s – Trials and simulations. FOA-R--99-01143-311--SE. FOA, Tumba, April 1999. (In Swedish)

Ågårdh, L., Magnusson, J. and Hansson, H., High strength concrete beams subjected to impact loading - An experimental study, FOA-R--99-01187-311--SE, FOA, Tumba, 1999.

APPENDIX: EQUATIONS

Table A1. General parameters and their relationships.

Parameter	Definition/Relationship
Sound velocity	c
Mass	m
Volume	v
Stress	σ
Density	$\rho = m/v$
Initial density	$\rho_0 = m/v_0$
Strain rate	$\dot{\varepsilon} = \varepsilon/t$
Bulk modulus	$K = \rho \cdot c^2 = \frac{E}{3(1-2\nu)}$
Poisons ratio	$\nu = \frac{E}{2G} - 1$
Young's modulus	$E = \sigma/\varepsilon = 3K(1-2\nu) = 2G(1+\nu)$
Shear modulus	$G = \frac{E}{2(1+\nu)}$
Compression	$\mu = \frac{\rho}{\rho_0} - 1$
Linear EOS	$P = \mu \cdot K$
Polynomial EOS	$P = A_1\mu + A_2\mu^2 + A_3\mu^3$

APPENDIX: GLOSSARY AND DEFINITIONS

Material definitions

Aggregate	Crushed rock or stone material in concrete, normally different type of granites.
HNS	(High) Nitrogen alloyed Steel has normally a content of 0.4 to 1.0 % nitrogen.
HPC	High Performance Concrete is normally concrete with an uni-axial compressive strength greater than 80 MPa.
WC	Tungsten carbide.

Numerical methods

ALE	For the Arbitrary Lagrange Euler formulation it is possible to define the relaxation of the elements, describing the behaviour of the elements. The behaviour of the elements can be varied from fixed elements (Euler) to elements that follows the material (Lagrange).
Element	For numerical analysis the material are divided in small cells, i.e. brick elements for a three dimensional model.
Erosion	A numerical erosion or kill algorithm is normally used to delete heavily distorted elements when the Lagrange formulation is used.
Euler	Euler formulation is characterised by a fixed element mesh, and the material is instead transported through the elements during the deformation.
Mesh	A part of the model that is divided into elements.
Lagrange	For the Lagrange or material formulation the elements deforms together with the material. The material is located to the same element during the simulation.
SPH	Smooth Particle Hydrodynamics is a meshless formulation for the geometry description of the model. The material is located to spheres that are linked together and builds up the geometry. During the simulation the material is located to the same nodes.

Other definitions

Ballistic limit	Normally the impact velocity at which half of the projectiles penetrates the target.
AP	Armour piercing ammunition, normally with steel or tungsten carbide (WC) core.